THE ASTROPHYSICAL JOURNAL, 406:97–111, 1993 March 20

A MULTIWAVELENGTH STUDY OF THE ERIDANUS SOFT X-RAY ENHANCEMENT

D. N. BURROWS,[1] K. P. SINGH,[2] J. A. NOUSEK,[1] G. P. GARMIRE,[1] AND J. GOOD[3]

Received 1992 July 9; accepted 1992 September 23

ABSTRACT

We present soft X-ray, N_H, and IR maps of the Eridanus soft X-ray enhancement. Soft X-ray maps from the *HEAO 1* A-2 LED experiment, processed with a maximum entropy method (MEM) algorithm, show that the enhancement consists of two distinct components: a large hook-shaped component and a small circular component at different temperatures. Both of these are located in "holes" in the IR emission, and they correspond to N_H features at very different velocities. The dust surrounding the X-ray enhancements appears to be associated with several high-latitude molecular clouds, which allow us to obtain a probable distance of ~ 130 pc to the near edge of the main enhancement. The total power emitted by the hot gas is then $\sim 10^{35}$–10^{36} ergs s^{-1}. We consider alternative interpretations of these objects as adiabatic supernova remnants or as stellar wind bubbles and conclude that they are more likely to be stellar wind bubbles, possibly reheated by a SN explosion in the case of the main, hook-shaped object.

Subject headings: infrared: interstellar: continuum — ISM: individual (Eridanus) — ISM: molecules — supernovae remnants — X-rays: interstellar

1. INTRODUCTION

The Eridanus enhancement [$(l, b) \approx (200°, -42°)$] is a well-known feature of the soft X-ray background. It is present in the map of Williamson et al. (1974) and was first identified as an object of interest by Naranan et al. (1976), who interpreted the X-ray enhancement as the hot interior of an old supernova remnant, based on positional coincidence with an expanding H I shell (Heiles & Habing 1974) and Hα filamentary loops (Sivan 1974). Heiles (1976) discussed a large, expanding H I shell with kinetic energy of $\sim 4 \times 10^{50}$ ergs that coincides with the X-ray enhancement. Far-UV emission associated with Hα filaments in this region may also be due to a supernova shock (Paresce, Jakobsen, & Bowyer 1983; Murthy et al. 1992). The X-ray enhancement has also been discussed by Long et al. (1977). Nousek et al. (1982), and Singh et al. (1982). It is present on the all sky maps of McCammon et al. (1983) at energies between ~ 0.1 and ~ 0.7 keV and has a hook-shaped appearance on the *SAS 3* C-band map (Marshall & Clark 1984) and the *HEAO 1* C-band map (Garmire et al. 1992).

The most extensive analysis of this object is provided by Reynolds & Ogden (1979), who studied faint Hα emission from the Eridanus enhancement. They found line splitting in Hα and [N II] emission from the direction of the enhancement consistent with emission by an expanding shell and concluded on the basis of their data plus previous optical, Hα, X-ray, and 21 cm results that a large cavity extends from the Ori OB1 association well into Eridanus. They suggested that the cavity, which they found to have an angular size of 47° × 33°, was produced by stellar winds and/or a series of supernova explosions originating in the Ori OB1 association.

We present X-ray maps of the Eridanus enhancement with the highest spatial resolution and sensitivity to date. The maps, in three soft X-ray bands, were prepared using the maximum entropy method (MEM) with data from the low-energy detectors (LEDs) of the *HEAO 1* A-2 experiment. The hook-shaped feature is clearly present on these maps in both the $\frac{1}{4}$ keV data (L1 and L2) and the 0.6 keV data (M1); we will refer to it as EXE1 (Eridanus X-ray Enhancement 1). A second feature at $(l, b) = (210°, -43°)$ is seen only in the $\frac{1}{4}$ keV data; we refer to it as EXE2. Comparison of the X-ray maps with N_H maps suggests that the two X-ray features are associated with different velocity components of the neutral gas. The smaller object, EXE2, is outlined by receding neutral gas spanning ~ 40 km s^{-1} in velocity and has an X-ray temperature of $\sim 1.5 \times 10^6$ K. The larger object, EXE1, is associated with approaching neutral gas spanning up to ~ 55 km s^{-1} in velocity and is anticorrelated in a fairly detailed way with a convoluted cavity apparent in 60 and 100 μm IR maps. It has an X-ray temperature of $\sim 2.2 \times 10^6$ K. These could represent independent supernova remnants superposed along the line of sight, interacting supernova remnants, or stellar wind bubbles. We discuss the implications of these scenarios and conclude that EXE2 is probably a stellar wind bubble, while the most likely model for EXE1 is a nearby superbubble blown by the winds of the Orion OB1 association and possibly reheated by supernovae.

2. DATA

2.1. *LED X-Ray Observations*

The Eridanus X-ray enhancement was scanned from 1977 August 17 to 1977 September 25, and again from 1978 January 14 to 1978 March 19, by the low-energy detectors (LEDs) of the *HEAO 1* A-2 experiment. Details of the *HEAO 1* A-2 experiment are given in Rothschild et al. (1979). The LEDs were four-layer multiwire proportional counters with thin polypropylene windows and propane counting gas. Incident X-rays were detected in the first three layers. The second and third layers were combined electronically and are referred to as the middle layer. The X-ray data reported here were collected by LED1, which has two coaligned mechanically collimated fields of view (1°.55 × 2°.95 [FWHM] and 2°.92 × 2°.80 [FWHM]), triangular in two dimensions. The collimators were mounted with the centers of the fields of view perpendicu-

[1] Department of Astronomy and Astrophysics, Penn State University, 525 Davey Lab, University Park, PA 16802
[2] X-Ray Astronomy Group, Tata Institute of Fundamental Research, Homi Bhabha Road, Bombay 400 005, India
[3] Infrared Processing and Analysis Center, California Institute of Technology, M/S 100-22, Pasadena, CA 91125

lar to the spin axis, and data were collected as the detector scanned the sky while the spin axis was kept pointed toward the Sun.

The four layers of the LED and the individual anode wires in each layer were operated in anticoincidence with one another to reject contamination of the data by charged particle events (Rothschild et al. 1979). Additional contamination by low-energy electrons and other events unrelated to cosmic X-ray radiation were minimized using data exclusion criteria based on electron rate, solar zenith angle, and K_P index (Singh et al. 1987). A complete discussion of data processing, contamination removal, and calibrations of the LED data is given in Garmire et al. (1992).

Three broad pulse-height (PH) intervals were defined for this analysis. They are designed to permit a clear separation between low-energy ($\frac{1}{4}$ keV) X-rays and medium-energy (0.6 keV) X-rays, and to provide the best possible sensitivity to the energies of interest for this object. These bands are shown in Figure 1. Band L2 (low energy, layer 2) consists of events detected in PH channels 4–12 of the middle layer of the LED and is responsive to X-rays with energies between 0.20 and 0.28 keV. Band L1 (low energy, layer 1) consists of events detected in PH channels 4–7 of the front layer of the LED. It provides a softer low-energy band than L2, with significant response between 0.15 and 0.28 keV, but also has significant response to X-ray energies of 0.35–0.55 keV. Band M1 (medium energy, layer 1) consists of events detected in the front layer in PH channels 10–14 and is primarily a 0.6 keV band, sensitive from 0.4–0.9 keV, but with some response to $\frac{1}{4}$ keV X-rays. We note that these bands are specially defined for this analysis and differ from the "standard" *HEAO 1* LED energy bands used in Garmire et al. (1992). The middle-layer data (L2 band) are included in spite of the low sensitivity of the middle layer to $\frac{1}{4}$ keV X-rays because (1) they are relatively immune to the contamination sometimes seen in the front layer data and (2) they provide an independent data set that can confirm the reality of features seen in the L1 map.

The data obtained in these three PH bands were used to make X-ray maps of a 45° × 45° region centered at Galactic coordinates $l = 200°$, $b = -40°$, using a tangent plane (gnomonic) projection with $\frac{1}{2}°$ pixels. The X-ray data resulted from a large number of nearly parallel scans across the Eridanus enhancement. For each 10.24 s time interval, the data collected from the two coaligned fields of view in each pulse height window were summed into the map pixel corresponding to the center of the combined field of view for that interval to create a map of X-ray counts. Similarly, the live time for each interval was summed into the map pixel corresponding to the look direction to create a map of exposure. The counts maps were divided by the exposure map to produce intensity maps for the three energy bands. These maps are presented in Figure 2 (Plates 7–9). The total exposure in the maps is 38,175 s.

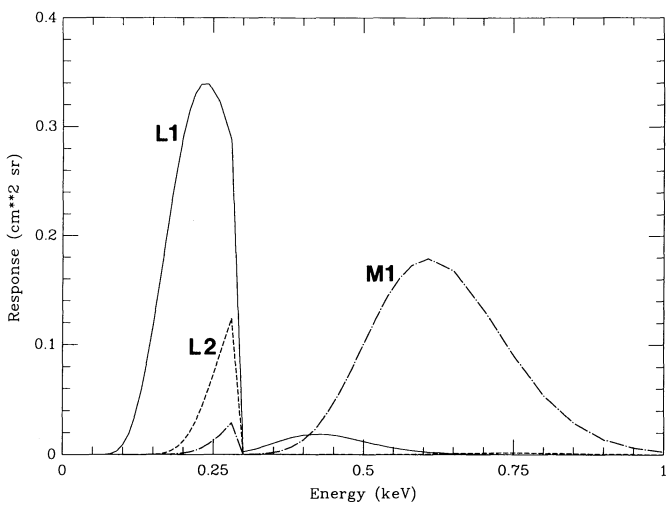

FIG. 1.—LED1 response curves for the PH bands used in this analysis. The response curves for the L1, L2, and M1 bands are shown by solid, dashed, and dot-dashed lines, respectively.

In order to smooth the data across gaps resulting from scans excluded because of contamination, and to maximize the spatial resolution of the maps, image reconstruction has been applied to the raw X-ray maps using MEM (Willingale 1981). In this method, a uniform X-ray intensity is assumed for the region of interest on the sky. This initial trial solution is convolved with the known collimator response function, and the result is compared with the observed data using the χ^2 statistic. (The collimator response used for the MEM technique was the sum of the two triangular response functions corresponding to the two fields of view.) A new trial solution is then obtained using an algorithm parameterized by Lagrangian multipliers (Gull & Daniell 1978; Willingale 1981). This process is iterated by incrementing the Lagrangian multipliers until an acceptable solution is obtained, as indicated by the minimum χ^2 achieved.

The central 32° × 32° regions of the observed X-ray maps were deconvolved from the collimator response using this procedure. A background region comprised of the border of the original data maps surrounding the central 32° × 32° region was needed for convolution of data points near the edge of the region. Because the information in this background region is incomplete due to a lack of coverage, an average value obtained from the observed portions of the background region was used for the entire background region. The distribution of intensities observed in this background region was broader than expected based on counting statistics and the assumption of a uniform sky intensity, indicating the presence of nonuniformities of 7%–10% of the count rate in this region. Under the assumption that the same nonuniformities are contained in the portions of the scans located in the central region, this average nonuniformity was added in quadrature to the uncertainty due to counting statistics for the purpose of determining χ^2 in the MEM. Pixels within the central region with no exposure were excluded from the calculation of the χ^2, but were filled in by the MEM if the collimator response from a good scan overlapped them.

The MEM maps of the three X-ray bands are shown in Figure 3. These maps, when convolved with the collimator response function and compared with the raw data, gave reduced χ^2 of 0.95, 1.08, and 0.95, respectively. The reality of map features can be verified by comparison of the MEM maps with the raw maps from which they were derived. Several spurious features on the MEM maps are due to incomplete coverage in the raw data. They include the region of low emission running along the scan direction just below the map centers and the abrupt northern edge at $b \approx -30°$ to $-33°$. The former is at least partially due to a band of missing data in the raw map running from $(l, b) = (182°, -41°)$ to $(227°, -47°)$, although there is a hint in both low-energy raw maps of a real minimum at $(l, b) \approx (199°, -47°)$. Spectral fits show that this minimum may be due to absorption of the $\frac{1}{4}$ keV X-rays by a

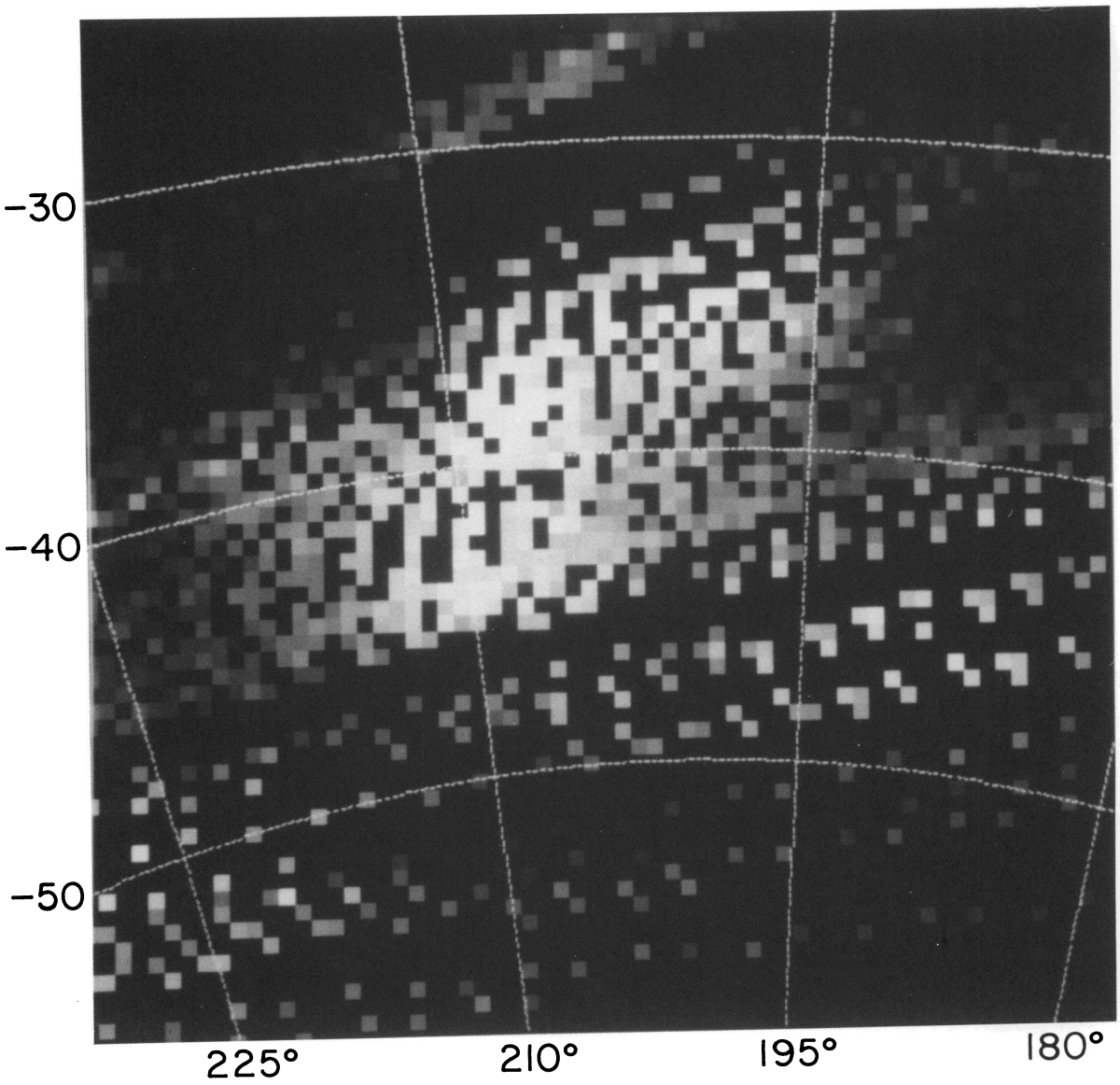

FIG. 2*a*

FIG. 2.—Gray-scale images of raw X-ray maps from the LED data in three energy bands. The grids are labeled in Galactic coordinates. (*a*) L1 map. (*b*) L2 map. (*c*) M1 map.

PLATE 8

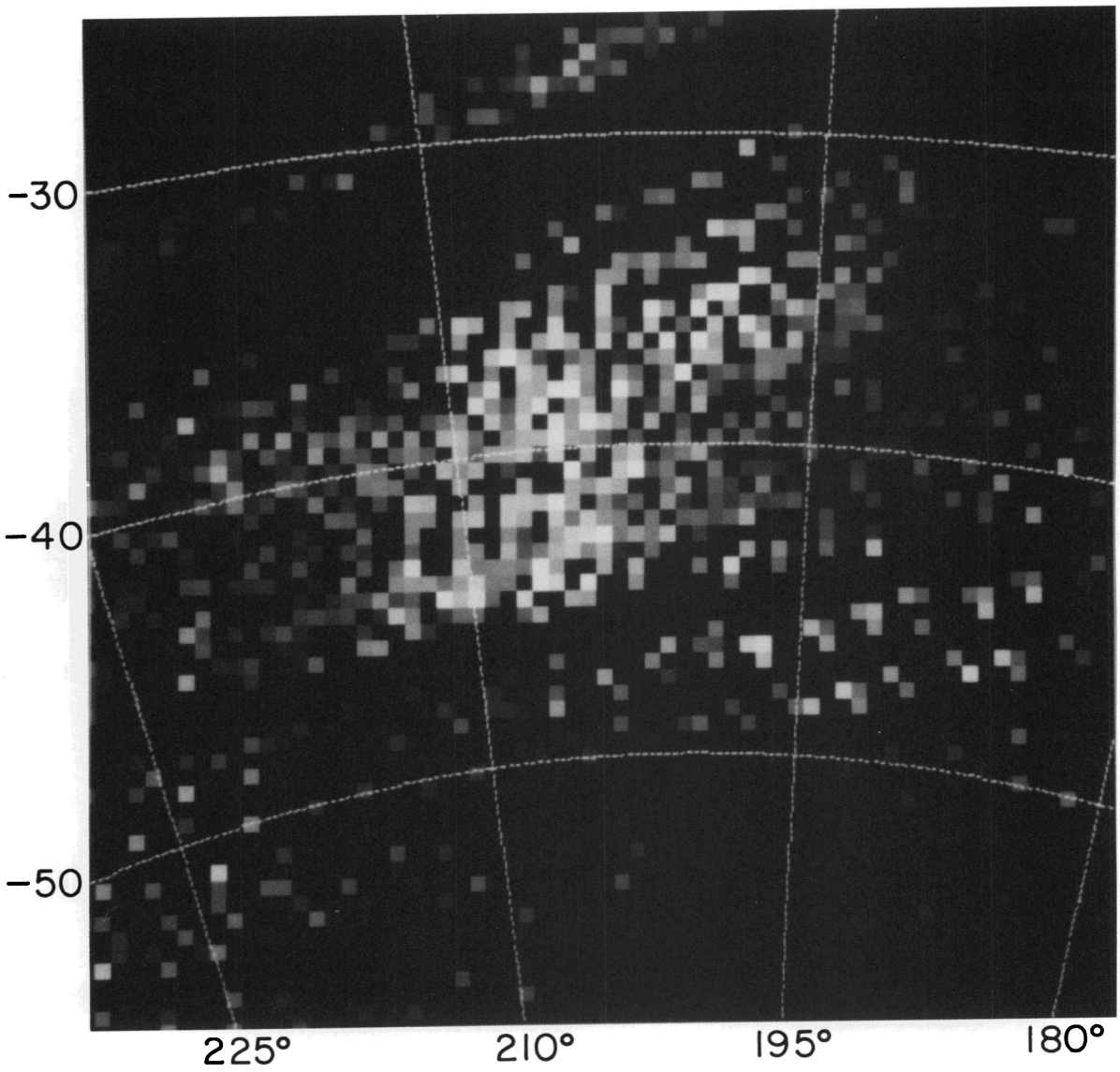

FIG. 2*b*

BURROWS et al. (see 406, 98)

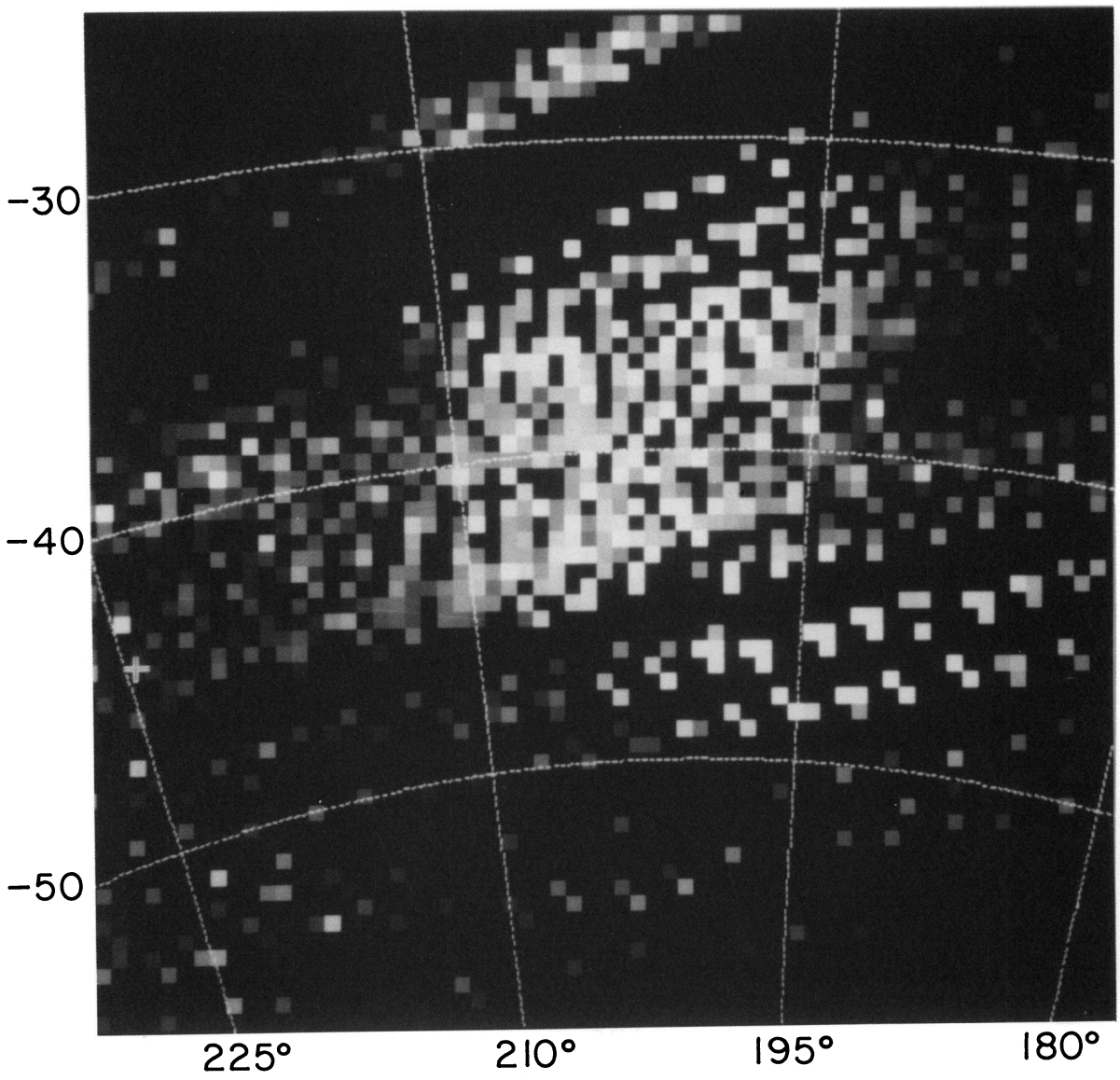

FIG. 2*c*

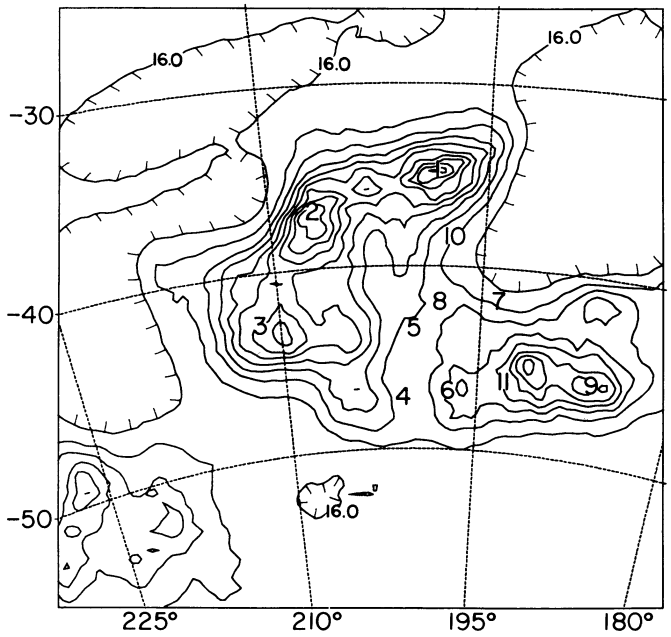

FIG. 3a

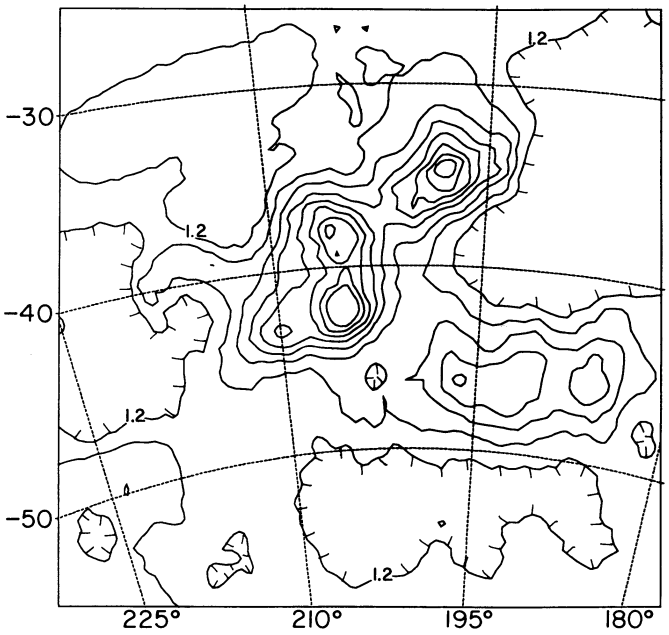

FIG. 3b

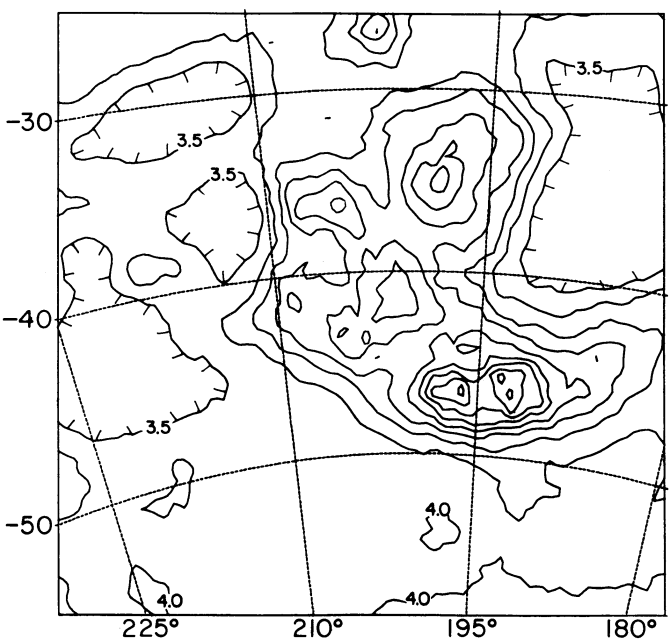

FIG. 3c

FIG. 3.—Contour plots of MEM deconvolution of the raw X-ray maps. (*a*) L1 map. The contour interval is 2.0 counts s^{-1}, and contours range from 16.0 to 34.0 counts s^{-1}. The numbers identify the positions for which spectral fits were performed (Table 1). (*b*) L2 map. The contour interval is 0.2 counts s^{-1}, and contours range from 1.20 to 2.80 counts s^{-1}. (*c*) M1 map. The contour interval is 0.5 counts s^{-1}, and contours range from 3.50 to 7.50.

filament of neutral gas. The northern boundary of the enhancement in the MEM maps is produced by a large band of missing data running from $(l, b) = (195°, -27°)$ to $(223°, -35°)$ and is probably not real. All three maps show a slight enhancement in the raw data north of this "dead band" at $(l, b) \approx (203°, -27°)$, but this enhancement was suppressed by the MEM reconstruction. It is reasonable to suppose that this enhancement is a continuation of the main enhancement to the south. This would be consistent with the conclusion by Reynolds & Ogden (1979) that the soft X-ray enhancement is associated with a large cavity extending all the way to the Ori OB1 association. Unfortunately, scans to the north of the region shown here are severely contaminated, and we cannot say from these data what the true extent of this feature is.

Finally, we point out that the L-band peak at $(l, b) = (186°, -42°)$ is due to HR 1099, which was discovered to be a soft X-ray source by the *Copernicus* satellite (White & Sanford 1978) and by the *HEAO 1* A-2 LEDs (Walter, Charles, & Bowyer 1978), but was not included in the Nugent et al. (1983) catalog of *HEAO 1* A-2 LED sources because of confusion with the extended emission of the Eridanus enhancement.

2.2. *IR Maps*

Infrared maps of the Eridanus region were generated from data collected by the *Infrared Astronomy Satellite* (*IRAS*), which is described in detail in Neugebauer et al. (1984). *IRAS* was placed in a nearly polar orbit and mapped 97% of the sky in small circle strips 0°.5 wide of constant solar elongation (near 90°) and running roughly from ecliptic pole to ecliptic pole. The solar elongation angle of the satellite was changed by 0°.25 for each scan, thus providing 50% overlap with the previous scan. Each area was scanned roughly 1 week and again 6 months after the original scans to provide confirmation of source reality on various time scales. (These confirmation scans were, in general, performed at different solar elongation angles and so are not parallel to the original scans.)

The focal plane contained 62 detectors in four wavelength bands (centered at 12, 25, 60, and 100 μm), providing wavelength-dependent angular resolution ranging from 1′ at 12 μm to about 5′ at 100 μm. Because this relatively high angular resolution is not convenient for comparison with the X-ray and 21 cm data, the IR data must be degraded to a resolution comparable to that of the other bands. An additional problem with the IR data is contamination from bright emission by interplanetary dust, which accounts for well over 90% of the

emission at 12 and 25 μm and well over 50% of the emission at 60 μm. A technique for removal of this zodiacal light from the IR data was required for this analysis.

Both requirements are met by using data from the Zodiacal History File, a standard *IRAS* data product in which data from the 62 detectors were averaged across the focal plane and in time to provide 0°.5 resolution data from the entire mission in a time-ordered series of scans (*IRAS* Explanatory Supplement 1986). These data can be co-added together to form 0°.5 resolution maps of any area of the sky. However, this procedure does not allow for correct zodiacal light subtraction from such maps. Because the zodiacal emission arises from a dust cloud through which the Earth moves, its intensity varies with the time of year and with the details of the satellite's pointing. Thus, raw maps will have severe artifacts in the form of an ecliptic equatorial bulge and longitudinal variations due to the viewing geometry, and these will be different for data taken during different confirmation scans of the same part of the sky. These artifacts are therefore very difficult to disentangle from co-added maps and must instead be removed from the original strip scans *before* they are co-added to form a map.

In principle the zodiacal light could be removed by constructing a model of its intensity and subtracting this from the data. However, calibration artifacts and other sources of contamination are also present in the data and would not be suppressed by this method. Since we are interested in observing emission from dust on angular scales of several degrees, we chose to empirically remove the large-scale variations from the individual strip scans before image generation. Small-scale structure must be preserved in this process, because the noise in these data is negligible compared to the real structure on the sky.

Unfortunately, a true high-pass filter does not work because the ecliptic emission, while quite smooth over most of the sky, has somewhat of a cusp near the ecliptic equator. Instead, a smooth fit to the zodiacal background was subtracted from each scan. Since all positive excursions in the data are considered to be real, the background curve was fitted to the lower envelope of the data. The curve used was a cubic spline under tension; this provides a generalized smooth curve which makes no assumptions about the shape of the data. The effective spatial frequency content of the curve is controlled by the placement of the control points for the spline. We used control points spaced every 15° along the scan, which had the effect of limiting the spatial frequencies in this background curve to have wavelengths longer than about 7°.

The curve was fitted to the data using a nonlinear least-squares fitting algorithm with the amplitudes of the control points as free parameters. In order to force the curve to fit the lower envelope of the data, the uncertainty for each data point was artificially set to a value proportional to its distance from the curve. This distance varies as the curve adjusts itself to the data, but since the nonlinear least-squares algorithm is an iterative process, this introduces no problems. Each strip scan in the Zodiacal History File was processed in turn: the control point amplitudes were determined, and the spline curve was subtracted from the data for that strip scan.

The result of this fitting is a residual Zodiacal History file which has the same form as the original but in which a smooth background has been removed from each scan. No artificially negative regions have been created, and strong positive spikes have effectively been ignored. The spatial frequency content of the curve removed is variable but roughly consists of just frequencies longer than 1/(7°). These data were then co-added into images with the same pixel size, projection center, and projection type as the X-ray data.

The resulting IR maps are shown in Figure 4. The bright stripe running diagonally across the 60 μm map from (190°, −46°) to (213°, −50°) is an instrumental artifact. The anticorrelation with the X-ray maps is striking. The X-ray enhancement fills in an apparent void in the IR emission, suggesting that the X-ray gas fills a cavity bounded by dusty cool gas. The X-ray enhancement curves around a prominent IR feature shaped like an arrowhead which is associated with a neutral hydrogen cloud seen at 21 cm and a Lynds dark cloud (L1569) with a molecular core (MBM 18). This accounts for the "hook-like" appearance of the X-ray feature. The relationship between the X-rays and IR emission is discussed further below.

2.3. N_H Maps

We produced maps of the neutral hydrogen column density for this part of the sky in velocity cuts ranging from -100 km s^{-1} to $+100$ km s^{-1} and spaced by 5 km s^{-1}, using 21 cm data from the Bell Labs 21 cm survey (Stark et al. 1992), which was made with the Crawford Hill 20 foot horn reflector. The telescope beam has a FWHM of 2° at 21 cm and has most of the power concentrated into the main beam with very small sidelobes, making it capable of very sensitive N_H measurements with little contamination compared to surveys using paraboloidal telescopes. The 21 cm data were oversampled in R.A. ($\frac{1}{4}$ beamwidth spacing) but undersampled in declination (1 beam width sampling). This problem is exacerbated when we cast the data into maps using the same projection and pixel size as the X-ray maps. The N_H maps were grossly undersampled because the spacing of the 21 cm data is coarse compared to the pixel size. In order to permit comparison between the X-ray and 21 cm data, the N_H maps were median smoothed, interpolated across data gaps, and then smoothed again with a 5 × 5 pixel boxcar average. Three of the resulting maps are shown in Figure 5. Column densities quoted in this paper were taken from unsmoothed maps of N_H.

3. ANALYSIS

3.1. X-Ray Spectra

X-ray spectral analysis of diffuse emission requires a thorough understanding of the detector response function and of the intensity and spectral shape of any contamination present. Fink (1990) has performed an exhaustive reanalysis of all of the preflight and in-flight calibration data for the LED1 detector used here, which revealed several errors in detector parameters and changes in the detector performance during the mission that were not accounted for in previous work. The result of this analysis is a definitive set of detector parameters as a function of date throughout the mission which are used to generate exposure-weighted LED response matrices for a given observation. This procedure was tested by fitting LED1 data from the North Ecliptic Pole (Garmire et al. 1992), which was scanned on every day of the mission and therefore presents the most difficult challenge to spectral fits, both because it exhibits the complete range of gain variations and because the large exposure time (9621 s) results in very small statistical uncertainties. The success of these spectral fits gives us confidence in our revised response matrices. Details of LED spectral fitting and contamination removal can be found in Garmire et al. (1992).

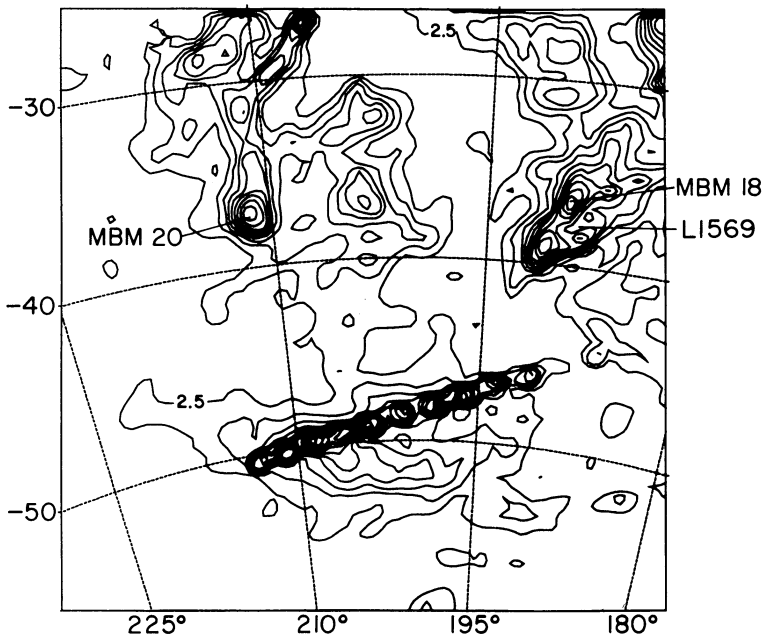

FIG. 4a

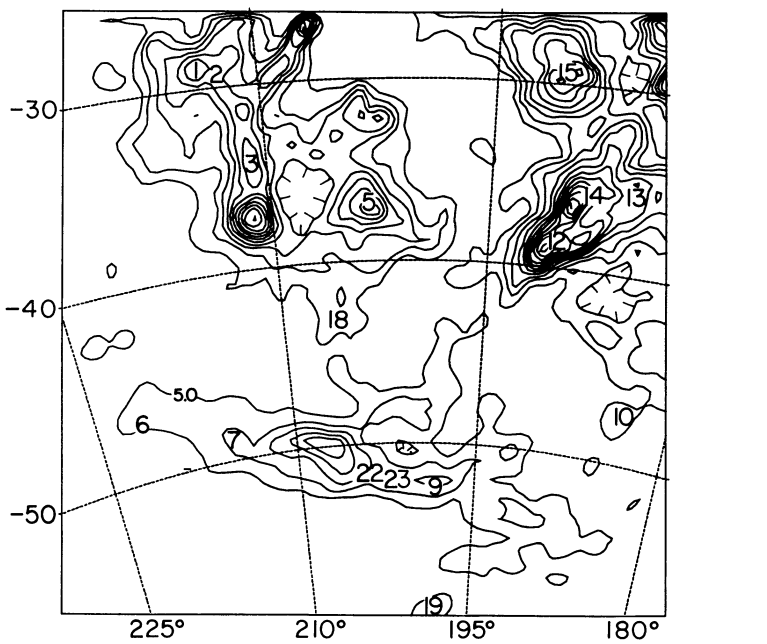

FIG. 4b

FIG. 4.—Maps of infrared emission. See text for processing details. (*a*) 60 μm map. The contour interval is 2.5 MJy sr^{-1}, with contours ranging from 2.5 to 27.5 MJy sr^{-1}. The positions of the high-latitude molecular clouds MBM18 and MBM20 are shown, as is the dark cloud L1569. The bright stripe running diagonally across the 60 μm map from (190°, −46°) to (213°, −50°) is an instrumental artifact. (*b*) 100 μm map. The contour interval is 5.0 MJy sr^{-1}, with contours ranging from 5.0 to 60.0 MJy sr^{-1}. Numbers identify the positions for which spectral fits were performed (Table 3).

We have performed spectral fits to the X-ray data from selected regions of the Eridanus enhancement (shown in Fig. 3*a*), using both single-temperature and two-temperature equilibrium models (Raymond & Smith 1977, 1990). These regions were selected to sample the parameters (temperature and absorbing column density) of the bulk of the hot gas, to measure those parameters in directions that appear to be absorbed based on the morphology of the emission, and to examine regions that appear to be unusual compared to the overall enhancement. The data from these regions were accumulated from the LED1 front layer for the combined fields of view, using all observations made with the field of view centered within 3° of the indicated positions. Background regions on both sides of the enhancement were used for calculating background spectra, which were averaged and subtracted from the spectra for each target region. An additional background region was processed in the same way to verify that the background subtraction was adequate. In some cases, high-energy

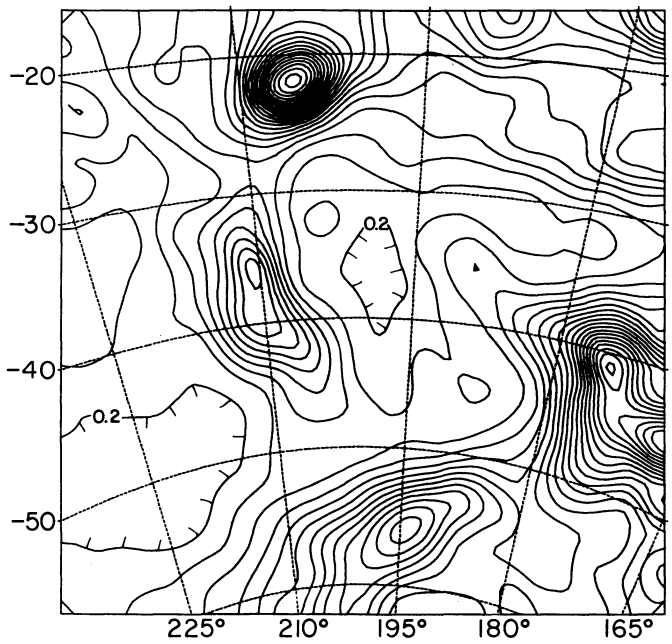

FIG. 5a

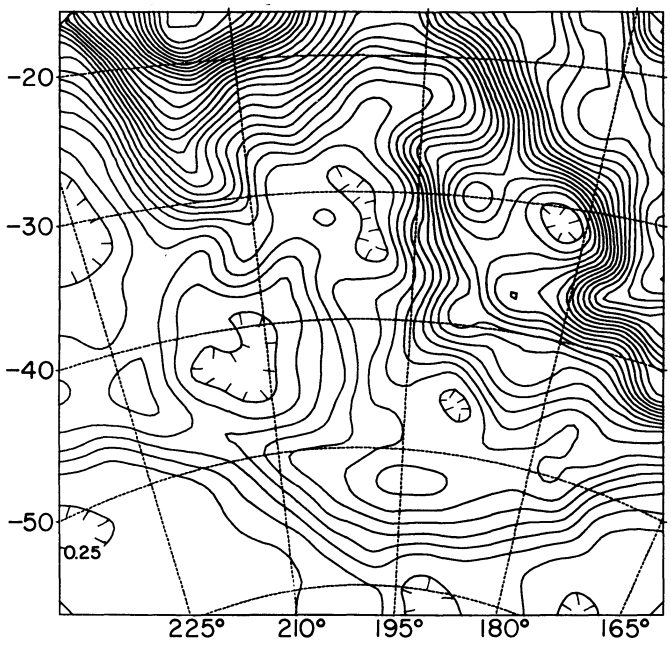

FIG. 5b

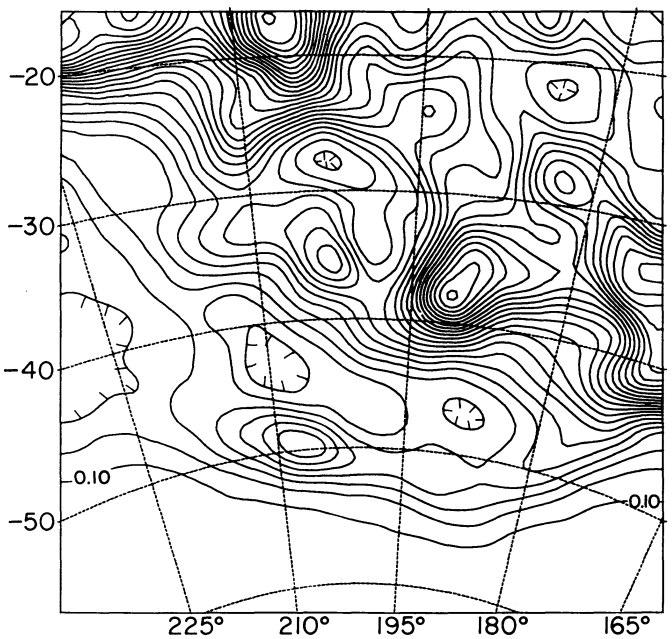

FIG. 5c

FIG. 5.—Maps of N_H. (*a*) -15 to -5 km s^{-1}. The contour interval is 10^{19} cm^{-2}, with contours from 0.20 to 2.30 $\times$ 10^{20} cm^{-2}. (*b*) 0 to $+10$ km s^{-1}. The contour interval is 0.25 $\times$ 10^{20} cm^{-2}, with contours from 0.25 to 8.75 $\times$ 10^{20} cm^{-2}. (*c*) $+15$ to $+20$ km s^{-1}. The contour interval is 10^{19} cm^{-2}, with contours from 0.10 to 2.80 $\times$ 10^{20} cm^{-2}.

channels were discarded or binned together to improve the fits, resulting in a varying number of spectral points per observation. Results are given in Tables 1 and 2.

Table 1 lists the results of the single-temperature fits, which obtained satisfactory results for points 3, 4, 7, 9, and 10. For those points, the 90% confidence limits (using the method of Lampton, Margon, & Bowyer 1976) on the temperature and N_H are given in the table. The remaining points were fitted with two thermal components, and the results are listed in Table 2. The 90% confidence limits on the temperatures of both components and on the N_H are given there. The single-temperature fits give the most reliable indication of the temperature and N_H toward the various directions. The two-temperature fits demonstrate that the remaining points can be fitted with an appropriate input spectrum and allow us to determine confidence limits on the interesting parameters, and the high temperature of the second component indicates that these directions require a broader range of incident energies than the other points. However, we do not attach any physical significance to this high temperature; instead, we believe that the second component indicates that modeling the emission by a single equilibrium model is inappropriate, and that it is likely that the emitting gas is either not isothermal or is not in equilibrium.

3.2. *X-Ray Morphology*

The X-ray and IR maps present several interesting morphological clues to the relationship between the hot and cold gas in this direction. Figure 6 (Plates 10–11) shows the X-ray MEM maps with 100 μm contours overlaid so that the relationship between the hot and cold gas is clear. A false color three-band image is shown in Figure 7 (Plate 12). In this photograph the 100 μm map is represented by red intensity, the L1 map by green intensity, and the M1 map by blue intensity.

Perhaps the most striking difference between the L1 and M1 maps is the dark band in the L1 map centered at $\sim$(200°, -46°) that splits the low-energy portion of the enhancement in two. Although this occurs near a gap in the data that produces a minimum in the M1 band map, the latter is roughly parallel to the scan direction, as one would expect, while the low-energy dark lane is at an angle of $\sim$80° to the scan direction. Inspection of the raw data (Fig. 2) confirms that this dark lane is present in the raw data and is not an artifact of the MEM reconstruction. The coincidence of faint IR and Hα filaments

PLATE 10

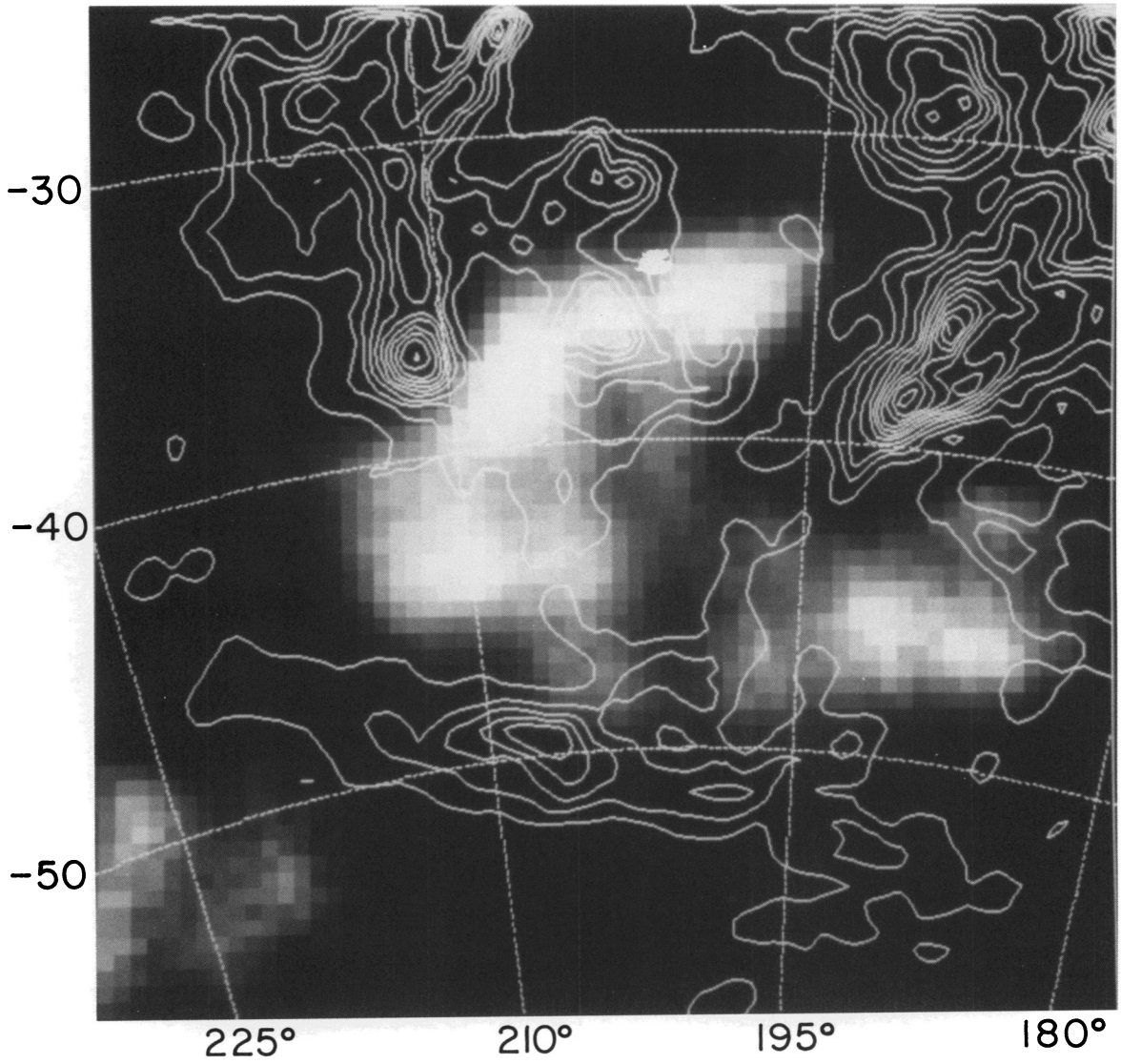

FIG. 6a

FIG. 6.—X-ray maps with 100 μm contours overlaid. (*a*) L1 map. (*b*) M1 map

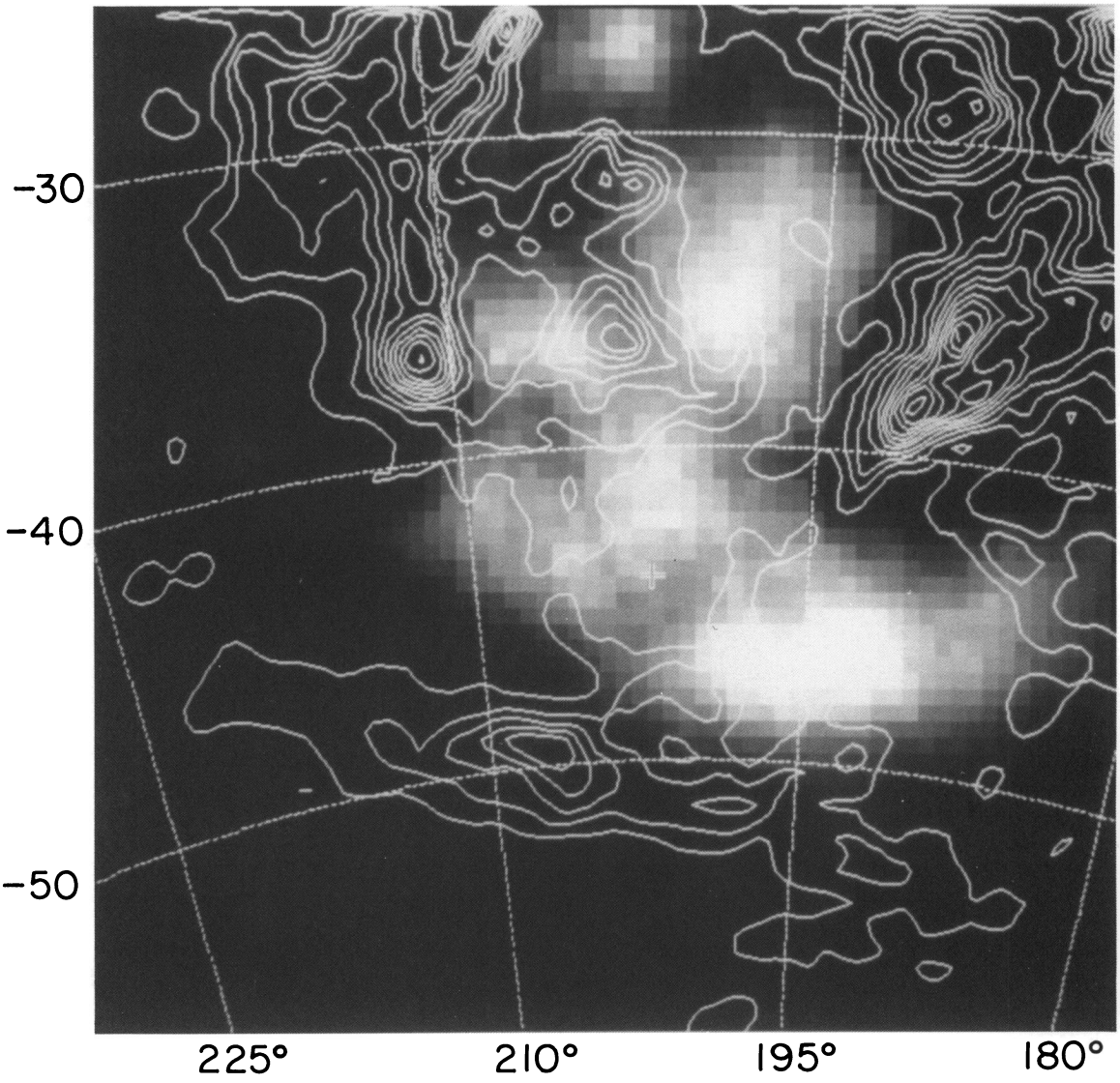

BURROWS et al. (see 406, 102)

PLATE 12

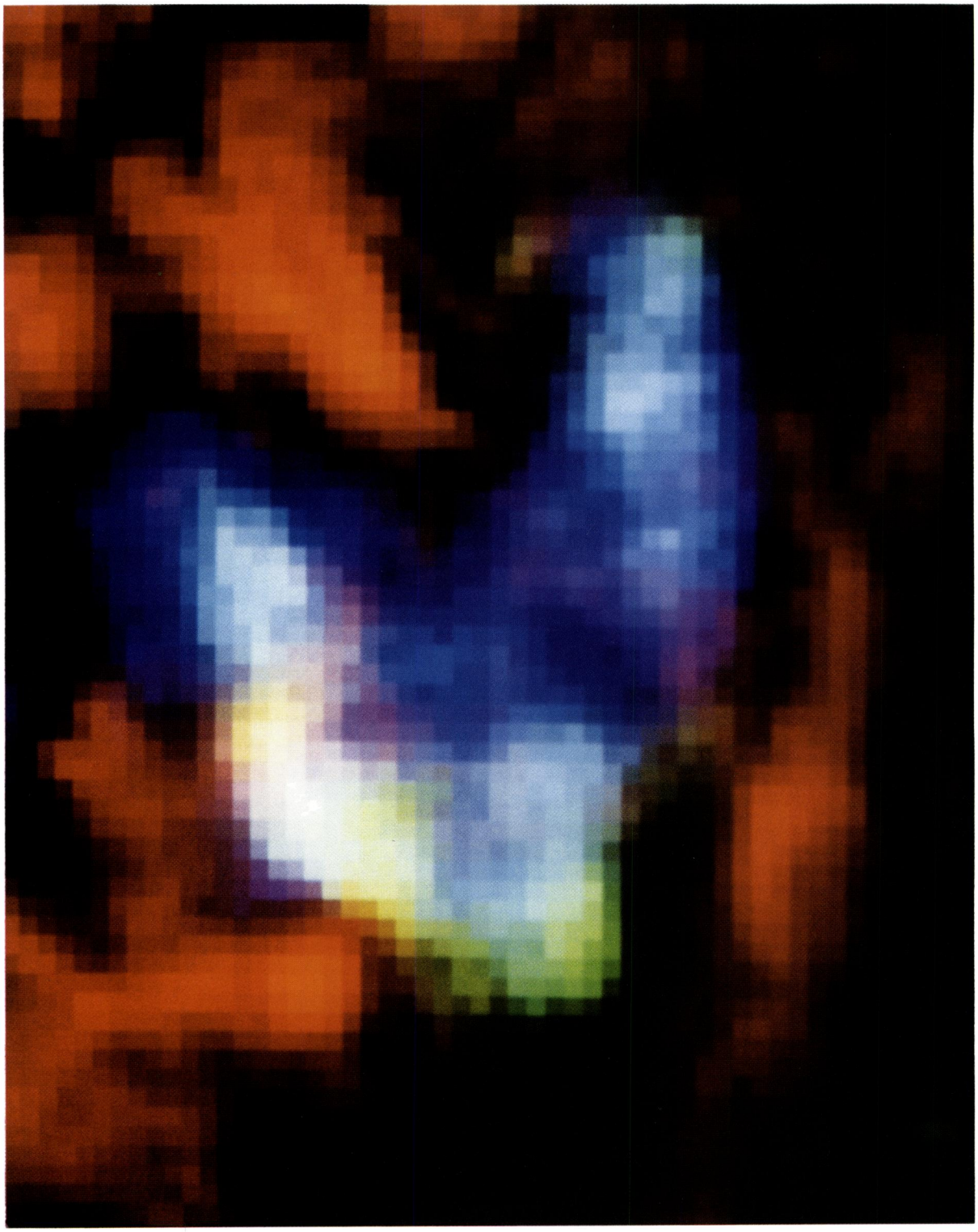

FIG. 7.—False color multiband image of Eridanus. The 100 μm map is shown in red, the L1 band map is in green, and the M1 band map is in blue.

TABLE 1

SINGLE-TEMPERATURE X-RAY SPECTRAL FITS[a]

Region	(l, b)	EM (10^{-3} cm^{-6} pc)	log T	N_H (10^{20} cm^{-2})	χ^2_{min}	d.o.f.
1.....	(198, −35)	6.13	6.34	0.2	50.8	24
2.....	(207, −37)	4.7	6.32	0.0	55.6	17
3.....	(212, −43)	2.84	$6.18^{+0.04}_{-0.16}$	$0.0^{+1.6}_{-0.0}$	26.8	24
4.....	(201, −47)	6.27	$6.42^{+0.04}_{-0.04}$	$0.10^{+0.5}_{-0.1}$	26.6	24
5.....	(199, −43)	5.48	6.37	0.57	36.6	24
6.....	(197, −47)	7.63	6.41	0.22	31.6	24
7.....	(193, −42)	2.83	$6.35^{+0.03}_{-0.04}$	$0.12^{+0.73}_{-0.12}$	18.2	17
8.....	(197, −42)	4.88	6.35	0.60	45.1	24
9.....	(186, −46)	5.6	$6.31^{+0.035}_{-0.08}$	$0.08^{+0.92}_{-0.08}$	24.5	24
10.....	(197, −38)	4.72	$6.37^{+0.02}_{-0.03}$	$0.10^{+0.40}_{-0.10}$	25.6	18
11.....	(193, −47)	8.7	6.39	0.34	43.2	24

with this dark lane, together with the fact that it is present in the low-energy map but not in the high-energy map, suggests that it may be caused by absorption in an intervening filament of partially ionized gas.

This interpretation is borne out by the spectral fits discussed above. The dark lane in the L1 map includes the data (points 5 and 8 in Tables 1 and 2) with the largest X-ray absorption column densities found for any of the points we examined. For the most part, N_H values are consistent with zero across the enhancement, and the best-fit values correspond to small optical depths at these energies (the effective absorption cross section at $\tau = 1$ for the L1 band, assuming a thermal spectrum with parameters from Table 1, is $\sim 0.8 \times 10^{-20}$ cm^2). This is not true, however, of points 5 and 8, which have significant absorption (on the order of an optical depth to $\frac{1}{4}$ keV X-rays, but with large uncertainties). These points lie on or near an IR filament with 100 μm intensity of ~ 6 MJy sr^{-1}. For a typical high-latitude ratio of 100 μm intensity to 21 cm column density of 0.85×10^{-20} cm^2 MJy sr^{-1} (Boulanger & Pérault 1988), this corresponds to a column density of $\sim 7 \times 10^{20}$ cm^{-2}. (Because absorption of L1 band X-rays is primarily due to H and He, the existence of an ionized component may result in a somewhat lower effective column density for X-ray absorption.) The lack of detailed agreement between the column density derived from the X-ray absorption and that derived from the IR emission may be due to the ionization state of the filament, to variations in the gas/dust ratio and/or interstellar radiation field, as reported by Boulanger & Pérault (1988) and Boulanger (1989) for nearby clouds, or to the fact that the large field of view of the X-ray detector dilutes the effect of absorption in this relatively thin filament. At any rate, this filament appears to represent roughly an optical depth in the L1 band, but is optically thin in the M1 band (which has an effective absorption cross section at $\tau = 1$ of about 0.15×10^{-20} cm^2).

Inspection of the right-hand boundary of the enhancement shows that the soft X-ray emission extends farther toward the northern edge of L1569 in the M1 band than in the L1 band. This can be seen in Figure 8 (Plate 13), which shows an X-ray "color" map (or band fraction map) formed by calculating the ratio

$$f_{M1} = \frac{I_{M1}}{I_{L1} + I_{L2} + I_{M1}}$$

for each pixel, where I_{L1}, I_{L2}, and I_{M1} are the excess intensities in the three X-ray bands after subtracting the minimum background rate measured away from the enhancement (15.1, 1.05, and 3.30 counts s^{-1} in the L1, L2, and M1 bands, respectively). The total rate map was calculated using a floor of 2.5 counts s^{-1} to prevent the ratio from blowing up in regions with very few excess counts. This band fraction map shows a hard rim on the northern boundary of L1569, which is suggestive of absorption by neutral gas associated with the dust producing the faint IR emission surrounding the dense molecular core of this dark cloud. On the other hand, the southern boundary of L1569 does not show a hard edge in the band fraction map, and the spectral fits for points 7 and 10 (on the edge of L1569) show no evidence for absorption. Thus, the evidence for X-ray

TABLE 2

TWO-TEMPERATURE X-RAY SPECTRAL FITS[a]

Region	EM_L[b]	log T_L	N_H (10^{20} cm^{-2})	EM_H[b]	log T_H	χ^2_{min}	d.o.f.
1.....	5.9	$6.3^{+0.03}_{-0.05}$	$0.4^{+0.5}_{-0.3}$	1.3	$7.17^{+0.24}_{-0.24}$	26.6	22
2.....	2.8	$6.18^{+0.1}_{-0.4}$	$0.0^{+3.0}_{-0.0}$	0.12	$6.55^{+0.60}_{-0.08}$	24.6	15
5.....	5.5	$6.33^{+0.05}_{-0.25}$	$0.9^{+1.6}_{-0.6}$	1.0	$7.17^{+0.48}_{-0.52}$	25.4	22
6.....	6.9	$6.39^{+0.04}_{-0.06}$	$0.3^{+0.6}_{-0.3}$	4.8	$7.8^{+\infty}_{-0.75}$	24.0	22
8.....	5.6	$6.26^{+0.08}_{-0.40}$	$1.4^{+5.0}_{-0.9}$	0.6	$7.05^{+0.20}_{-0.50}$	33.2	22
11.....	7.9	$6.37^{+0.03}_{-0.04}$	$0.5^{+0.60}_{-0.35}$	6.6	$7.8^{+\infty}_{-0.65}$	27	22

[a] Errors bars are 90% confidence limits.
[b] Units are (10^{-3} cm^{-6} pc).

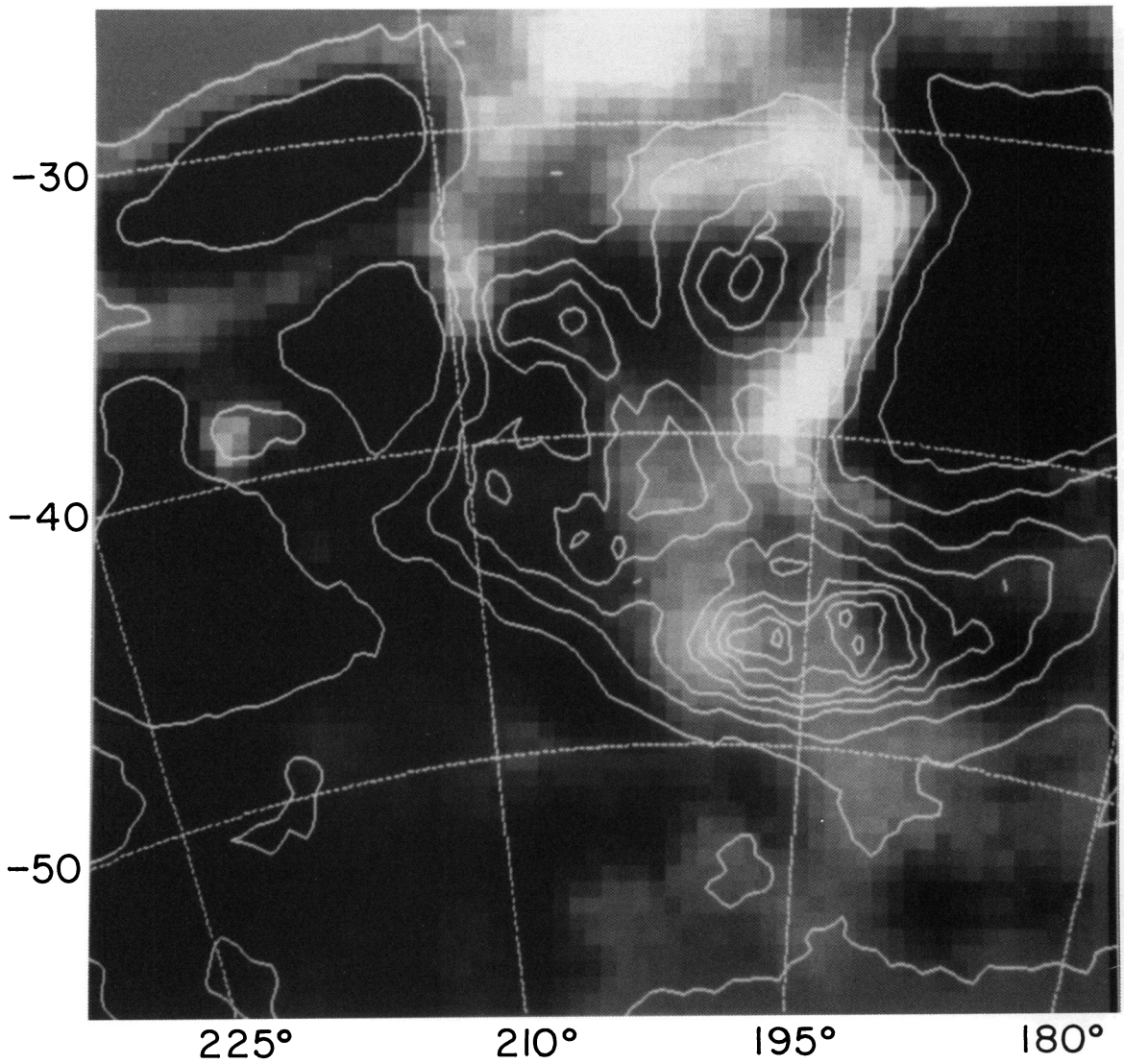

FIG. 8.—X-ray "color" map of Eridanus, with M1 contours overlaid. This is a map of the band fraction ratio, $f_{M1} = I_{M1}(I_{L1} + L_{L2} + I_{M1})^{-1}$. Faint regions are soft, which implies low temperature, while bright regions are relatively hard, which implies either high temperature or absorption.

absorption by L1569 must be considered to be marginal and somewhat inconsistent.

The $\frac{1}{4}$ keV peak at $(l, b) = (210°, -43°)$ (near point 3 in Table 1) has no corresponding peak in the M1 map, suggesting that it has a significantly softer spectrum than the main enhancement. This part of the enhancement is very soft on the band fraction map (Fig. 8) and green on Figure 7, indicating a soft spectrum. The spectral fits confirm this conclusion. Point 3 is significantly cooler (1.5×10^6 K) than the remainder of the remnant, which is characterized by temperatures near 2.2×10^6 K. Thus the M1 enhancement is characterized by a fairly uniform temperature, while the low-temperature component centered near point 3 is both spectrally and spatially distinct. We show below that the 21 cm data suggest that the latter is a separate object. As we said earlier, we will refer to the main M1-band enhancement as EXE1 and to the smaller L-band enhancement as EXE2 in subsequent discussion.

3.3. *21 Centimeter Data*

We have compared the N_H maps with the X-ray and IR maps to infer the kinematic behavior of the structures seen at those wavelengths. The N_H maps contain two large structures associated with the X-ray enhancements. Both appear to be cavities in the neutral gas, with rather poorly defined shell structures. These are discussed in some detail below. In addition to these cavities, the positive velocity maps also contain several clouds that appear to be associated with the cavities, including one that coincides in position with L1569 and which spans velocities of $+10$ km s^{-1} to $+30$ km s^{-1}. As we discuss below, this velocity range is consistent with optical absorption line studies of stars in this region.

Figure 5*a* shows the negative velocity cavity associated with EXE1. It is most clearly seen between -5 and -15 km s^{-1}, but is visible at velocities between $+5$ km s^{-1} and -50 km s^{-1}. It is irregularly shaped, and its shape and size vary with velocity, becoming a small circular hole at the most negative velocities. Its size decreases with decreasing velocity, suggesting that it may represent the near side of an expanding shell of neutral gas. If we assume that the gas seen in the edge of this N_H shell at its maximum extent is typical of the shell in order to estimate the shell properties, we can estimate the mass and kinetic energy of this shell. The filament that borders the X-ray enhancement along $l \sim 210°$ offers the best opportunity for measuring the shell column density, because it is well away from any confusing sources of foreground or background emission. This filament has a typical column density of $\sim 1 \times 10^{20}$ cm^{-2}. If we take the expansion velocity as 40 km s^{-1} (consistent with both the 21 cm data presented here and the Hα data of Reynolds & Ogden 1979), take into account the geometry for a line of sight tangential to a spherical shell, and use a factor of 1.4 for the total mass-to-hydrogen ratio, we derive the following (very uncertain) estimates of the H I shell parameters: density of $0.6 d_{130}^{-1}$ cm^{-3}, mass of $3000 d_{130}^2\ M_\odot$ and kinetic energy of $5 \times 10^{49} d_{130}^2$ ergs, where $d_{130} = (d/130$ pc). (In § 4.1 we argue that d_{130} is probably between 1.0 and 3.0.) However, if we use the column density of the "cap," which is only $\sim 3 \times 10^{18}$ cm^{-2} through the center of the cavity (-40 to -50 km s^{-1}), we obtain estimates of $n_s \approx 0.1 d_{130}^{-1}$ cm^{-3}, $M_s \approx 500 d_{130}^2\ M_\odot$, and $E_s \approx 0.8 \times 10^{49} d_{130}^2$ ergs. The uncertainty in these values is clearly very large. The discrepancy between the values found from the tangential filament and the cap could be explained either by a nonuniform shell density or by an elongated shell geometry. We discuss this further in § 4.6.

By comparison, Reynolds & Ogden (1979) found that the ionized shell has $n_e \approx 1.9 d_{130}^{-1/2}$ cm^{-3}, $M_s \approx 4500 d_{130}^{5/2}\ M_\odot$, and $E_s \approx 1.0 \times 10^{49} d_{130}^{5/2}$ ergs.

The second N_H cavity is associated with EXE2. It is present in all the positive velocity maps between $+0$ and $+40$ km s^{-1}, but is perhaps most clearly visible in the $+5$ to $+10$ km s^{-1} range (Fig. 5*b*), where it reaches its maximum size. At large positive velocities, the diameter of the cavity decreases, and the shell becomes very faint, while at negative velocities the shell becomes poorly defined and merges with other structures. This suggests that the structure may be the far side of an expanding shell. Again, assuming a spherically symmetric shell, we obtain a shell density of $0.3 d_{130}^{-1}$ cm^{-3}, mass of $500 d_{130}^2\ M_\odot$ and kinetic energy of $6 \times 10^{48} d_{130}^2$ ergs for a shell expansion velocity of ~ 35 km s^{-1}. (These numbers have uncertainties of at least 50%.) In this case, the tangential and central lines of sight provide similar estimates for the shell mass and kinetic energy, implying a more unifom or more spherical shell than we found for EXE1.

We have implicitly assumed in the preceding paragraphs that the N_H shells under discussion are two separate objects rather than the two sides of a single expanding shell. Since the central velocity of each appears to be near zero, this assumption requires some justification. First, these two N_H structures differ morphologically, in that the approaching shell has an elongated shape in the plane of the sky with angular size $25° \times 15°$ and has substantial column densities in well-defined bounding filaments. By contrast, the receding shell is nearly circular with a diameter of only 5° and has poorly defined edges with very low column densities. Second, the receding portion is centered just outside a filament that comprises the boundary of the approaching portion, an unlikely geometry for a single shell. Finally, the X-ray temperatures associated with the two structures are different. Based on their velocity differences and the different morphologies and spectra of the associated X-ray emission, we suggest that they represent two distinct objects, although we cannot rule out the possibility that EXE2 represents a small-scale blowout from the boundary of EXE1.

Our interpretation of these data differs from that of Heiles (1976), who assumed that the X-ray emission was associated with a single large expanding shell centered at a velocity of $\sim +20$ km s^{-1} with a radius of roughly 20°. The shell identified by Heiles is much larger than either of the features discussed above, although the Heiles shell is tangent to the negative velocity shell discussed here along a prominent Hα and IR filament at $b \sim -50°$ with $v \sim 10$–20 km s^{-1} (Verschuur et al. 1992) which appears to bound EXE1 in that region. Our X-ray data clearly show that the X-ray emission does not fill the Heiles shell; instead it is associated with two smaller cavities at different velocities which have much less energetic shells. In § 4 we consider several possible models for these objects: independent supernova remnants superposed coincidentally in the plane of the sky, interacting supernova remnants representing the breakout of a supernova cavity into a preexisting hot bubble, and stellar wind bubbles.

3.4. *IR Data*

Because of the evident morphological association of dust with the hot X-ray–emitting gas, we searched for evidence in the *IRAS* data that the hot gas was preferentially heating the dust near the edges of the cavity. We chose 23 positions in the vicinity of the X-ray enhancement, in locations ranging from

cloud centers to very faint filaments with 100 μm surface brightnesses spanning the range 0.9–10 MJy sr^{-1}, to perform quantitative measurements of the dust temperature. These positions are shown on the 100 μm map in Figure 4*b*. At each position we fit the surface brightnesses of the four *IRAS* bands using a two-temperature model of thermal dust emission for a power-law emissivity relation of index 2. The results for 18 of these positions are given in Table 3 (the remaining positions were contaminated by bad data or by bright sources, or did not produce acceptable fits). The mean temperature of the cold component for the first 16 points is 28.0 ± 1.7 K (1 σ uncertainty).

The last two points are located on an H I filament studied in detail by Verschuur et al. (1992), who found that the dust and gas for this filament appear to be separated by up to 0°.8. The H I filament is to the north of the IR filament, suggesting that their separation may be due to radiation pressure from the interior of the cavity. Verschuur et al. also found that the IR emission from the H I filament indicated a higher temperature than that from the IR filament. We find the same effect, with our points 22 and 23 indicating an average temperature of 33.6 K, or 5.6 K warmer than the rest of the dust for this part of the sky.

The warm component has a mean temperature of 368 ± 28 K (1 σ), excluding the points located on L1569, which are warmer than average, and point 18, which is unusually cool. We attribute the warm component, which contributes ~30%–50% of the total luminosity, to emission from small grains (Boulanger & Pérault 1988; Puget & Léger 1989), but assign no physical significance to the temperatures found, since these grains are not in equilibrium with the radiation field.

Use of a different emissivity index results in slightly different temperatures, but does not significantly change the conclusions above. For an index of 1, the temperatures are typically ~5.5 K warmer than those listed in Table 3 (but the difference varies with temperature).

With the possible exception of the Verschuur filament, we conclude that no significant temperature variations are present in our current maps. However, we note that temperature variations could be present on a finer angular scale and simply be masked by the size of our pixels. Small-scale temperature variations have been found for the cloud at (203°.3, −36°.8), which shows evidence of external heating (D. Van Buren 1992, private communication).

4. DISCUSSION

This region presents a complex (and fascinating) intermingling of large-scale features at many wavelengths. In spite of the accumulating data on this region, it is difficult to unambiguously disentangle this information to present a unified picture of the interactions. Several different scenarios appear to be consistent with much of our current data. We first discuss the observational data from all available wavelengths for EXE1 and EXE2 separately. We then consider three possible models of the region: X-ray emission from the interiors of (1) old SNR cavities or (2) stellar wind bubbles, superposed by chance along the line of sight, or (3) an interaction scenario in which EXE2 represents a young SNR breaking out of its birthplace and reenergizing the older cavity EXE1.

4.1. *EXE1: The Eridion Bubble*

The main diffuse X-ray feature comprising the Eridanus enhancement, EXE1, is evident in the X-ray maps spanning energies of 0.15–0.7 keV. This feature is prominently "hook-shaped," and comparison with the 100 μm map shows that the X-ray enhancement lies within an apparent cavity in the dust which is surrounded by faint IR filaments and several bright IR features.

The most notable of these bright IR features is L1569, which appears to nestle into the curve of the X-ray hook. A higher resolution *IRAS* image of this region is shown in Penprase et al. (1990); at higher resolution this cloud is seen to break up into a complex system of condensations and filaments dominated by linear filaments outlining its two long edges. Penprase et al. studied optical absorption lines in high-resolution spectra of six stars in the direction of this dust complex. They detected a variety of molecular species absorbing at LSR velocities of about 9–10 km s^{-1} and concluded that these absorption features were produced by the molecular cloud MBM 18. An additional velocity component at ~20 km s^{-1} was present in the Na D lines at a greatly reduced equivalent width. These

TABLE 3

TWO-TEMPERATURE IR SPECTRAL FITS

Region	(l, b)	12 μm (MJy sr^{-1})	25 μm (MJy sr^{-1})	60 μm (MJy sr^{-1})	100 μm (MJy sr^{-1})	T_1 (K)	T_2 (K)
1.....	(213.8, −28.4)	0.36	0.30	1.18	6.35	28.3	389
2.....	(212.3, −29.1)	0.18	0.15	0.90	4.67	29.0	392
3.....	(210.8, −34.1)	0.49	0.41	0.97	6.34	25.8	383
5.....	(203.1, −36.5)	0.39	0.37	1.12	7.27	26.1	350
6.....	(221.3, −46.5)	0.07	0.06	0.23	1.34	27.5	377
7.....	(215.4, −47.9)	0.10	0.07	0.41	1.96	29.8	424
9.....	(198.4, −51.8)	0.14	0.16	0.56	2.68	29.2	322
10.....	(183.4, −46.6)	0.11	0.11	0.38	1.83	29.5	358
12.....	(190.4, −38.6)	0.53	0.39	1.54	8.94	27.5	418
13.....	(185.4, −35.6)	0.20	0.16	0.83	5.84	25.8	396
14.....	(188.4, −35.9)	0.22	0.10	1.09	6.24	28.1	641
15.....	(190.5, −29.3)	0.39	0.34	0.87	6.57	24.5	374
16.....	(198.9, −25.3)	0.11	0.09	0.39	2.02	28.7	399
18.....	(205.5, −42.9)	0.18	0.33	0.37	1.37	28.0	253
19.....	(198.2, −58.3)	0.22	0.24	0.35	1.29	30.5	331
20.....	(206.1, −63.0)	0.11	0.10	0.20	0.88	29.7	361
22.....	(203.9, −51.3)	0.42	0.44	0.80	2.56	33.4	334
23.....	(201.6, −51.3)	0.22	0.20	0.76	2.63	33.8	362

velocities are consistent with the range of velocities in which this feature is seen at 21 cm. From photometric and spectroscopic distances to these stars, they derived an upper limit of 160 pc for the distance to this cloud, consistent with the distance of 130 ± 20 pc found by Franco (1988a, b) from photometry. We take 130 pc as the distance to L1569.

The association of EXE1 with this dust cloud allows us to place limits on the distance to the hot gas. As we discussed above, some of the faint filaments seen in the IR data appear to be absorbing X-rays from EXE1, and there is evidence that L1569 is also absorbing X-rays along its northern boundary. It is possible that the X-ray remnant is actually circular in projection on the sky, and that its apparent shape is due to absorption by L1569. The peak 100 μm brightness of L1569 is about 50 MJy sr^{-1}, corresponding to a column density of $\sim 6 \times 10^{21}$ cm^{-2}, or roughly nine optical depths to M1-band X-rays. Thus, L1569 is sufficiently optically thick to support this interpretation. This places EXE1 beyond L1569, or at a distance of at least 130 pc.

On the other hand, it is possible that the X-ray remnant is interacting with L1569. If so, the linear IR filaments running parallel to the edge of the cloud may be produced by shocks being driven into the cold cloud from the X-ray cavity. This interpretation is supported by the coincidence of a bright Hα filament with L1569, suggesting that a portion of the gas in this cloud is being directly illuminated by UV flux from the Ori OB1 association, which implies that there is very little neutral gas between the cavity and this cloud. The simplest interpretation is that the hot cavity is in direct contact with the cloud, but we cannot rule out the possibility of warm ionized gas between the cavity and the cloud. If they are in contact, the distance to the near side of the hot cavity is ~ 130 pc in this direction. For the present, we will adopt 130 pc as the most likely distance to the near edge of EXE1, but we will characterize its properties with an explicit distance dependence.

An upper limit to the distance can be found if there is a cloud in the direction of the X-ray enhancement that does *not* appear to absorb the X-rays. Such an object is seen at (203°.3, −36°.8) in the 100 μm map (Fig. 4*b*) and in the +15 to +20 km s^{-1} $N_{\rm H}$ map (Fig. 5). Although it is coincident with a local minimum in the M1 map, it coincides with a local *maximum* in the lower energy L1 map, and therefore cannot be associated with absorption. The cloud has a peak 100 μm brightness of 38.4 MJy sr^{-1}, which corresponds to 4.5×10^{21} cm^{-2} and represents many optical depths to the L1 band. We can therefore say with certainty that this cloud is not located on the near side of the X-ray enhancement. Instead of an absorption feature, the X-ray data in this direction suggest a temperature minimum, since the L1 band increases while the M1 band decreases at this point. This cooling in the vicinity of the dust cloud could be due to evaporation of the cloud if it is indeed embedded in the cavity. This interpretation is consistent with a more detailed analysis on a fine angular scale of the *IRAS* 12 μm/100 μm, 25 μm/100 μm, and 60 μm/100 μm ratios across this cloud, which peak at the edges of the cloud, suggesting an external heating source for this dust (D. Van Buren, 1992 private communication). This cloud may therefore hold the key to determining the distance to EXE1, if its distance can be determined accurately.

Other evidence for the distance comes from Hα observations. Reynolds & Ogden (1979) place the cavity at a distance of ~ 400 pc, based on their conclusion that the Hα emission is produced by the Ori OB1 association, which is 460 pc from the Sun. We take the distance to the Ori OB1 association as an upper limit to the distance to the far edge of EXE1.

Taking all of this into account, the most likely scenario is that EXE1 extends from L1569 (130 pc) to Ori OB1 (460 pc). Together with the angular diameter of this object, this suggests a structure elongated along the line of sight, with a semimajor axis of roughly 160 pc and a semiminor axis of 50–75 pc. Because this large cavity extends across the constellations Eridanus and Orion, we will refer to it as the Eridion Bubble for convenience. Emission from hot gas in the Eridion Bubble produces the X-ray feature we call EXE1 (the Eridanus Enhancement).

The X-ray flux of this object is found by integrating the observed count rate across the remnant and converting this total count rate to the equivalent incident flux, using model spectra corresponding to the spectral fits given in Table 1. The incident integrated flux for EXE1 is 2.9×10^{-8} ergs cm^{-2} s^{-1} (0.1–1.0 keV). Correcting this flux for intervening absorption, we obtain an X-ray luminosity for EXE1 of $6.7 \times 10^{34} d_{130}^2$ ergs s^{-1}. These values should be $\sim 28\%$ higher if the remnant is actually spherical and its hook-shaped appearance is due to absorption by L1569. These model-independent quantities are summarized in Table 4. We also include the density of the X-ray-emitting gas, determined from the average emission measure and average temperature of EXE1, and the thermal pressure of the interior of the Eridion Bubble. The derived density and pressure are rather large because of the small cavity size deduced from the angular diameter of the bubble under the assumption that the bubble is spherical. If the bubble is elongated along the line of sight as we have suggested, then the derived density is 0.004 cm^{-2}, and the pressure is 9000 cm^{-3} K.

4.2. *EXE2*

We now turn our attention to the second X-ray feature, EXE2, which is seen only in the $\frac{1}{4}$ keV bands. At the resolution of our X-ray maps, this object appears to be nearly circular,

TABLE 4

MODEL-INDEPENDENT PARAMETERS OF X-RAY ENHANCEMENTS

Parameter	EXE1		EXE2	
$\mathscr{F}_x$ (ergs s^{-1} cm^{-2})	2.9×10^{-8}		1.4×10^{-9}	
T_x (10^6 K)	2.13		1.57	
	$d = 130$ pc	$d = 400$ pc	$d = 130$ pc	$d = 300$ pc
$\mathscr{L}_x$ (ergs s^{-1})	6.7×10^{34}	6.3×10^{35}	2.8×10^{33}	1.5×10^{34}
R_s (pc)	22.6	69.5	5.7	13.1
n_x (cm^{-3})	0.011	0.0064	0.016	0.010
$P_{\rm th}$ (cm^{-3} K)	23400	13600	24800	16300

suggesting emission from a roughly spherical region of hot gas. As we noted earlier, the existence of a nearly circular hole with an expanding (but rather diffuse) shell in the positive velocity N_H maps at this position suggests that this object is a second hot cavity.

The distance to this object is unknown. In principle, our X-ray spectral data should be able to provide information on the relative placement of EXE1 and EXE2 along the line of sight, since the H I filament that bounds EXE1 along $l \approx 208°$ nearly crosses the center of EXE2 and has a column density of about 1×10^{20} cm^{-2}. Unfortunately, our spectral data are not good enough to constrain the relative locations, since the allowable range of N_H for EXE2 is from 0 to 1.6×10^{20} cm^{-2}. Higher quality data from *ROSAT* could determine whether or not this N_H filament absorbs X-rays from EXE2.

If EXE2 is interacting with EXE1, then they are at the same distance, which we have argued is likely to be as close as ~ 130 pc. If these objects are not interacting, then EXE2 could be anywhere along the line of sight. However, it is unlikely to be more than 200 pc below the Galactic plane, which places an upper limit of ~ 290 pc on its distance. We therefore adopt 130 and 300 pc as characteristic distances that typify the likely range of possible values.

The X-ray luminosity of EXE2 is calculated in the same way as above, using the spectral data for point 3 (see Table 1). The incident integrated flux is 1.4×10^{-9} ergs cm^{-2} s^{-1} (0.1–1.0 keV), which corresponds to an X-ray luminosity of $2.8 \times 10^{33} d_{130}^2$ ergs s^{-1}. The density in the cavity is $0.016 d_{130}^{1/2}$ cm^{-3}, and the pressure in the cavity is $25{,}000 d_{130}^{1/2}$ cm^{-3} K. These results are listed in Table 4.

4.3. *Two Supernova Remnants*

We now consider the hypothesis that EXE1 and EXE2 are two separate, noninteracting supernova remnants. We assume that the remnants are in the adiabatic phase (we show below that this assumption is reasonable). Using the relationship between the shock temperature, T_s, and the X-ray spectral temperature, T_x, given by Rappaport, Doxsey, & Solinger (1974), and the relations for the physical parameters of an SNR in the Sedov phase given by Hamilton, Sarazin, & Chevalier (1983), we can estimate the ambient density of the ISM, shock temperature, and velocity, and the age of each remnant. Casting these relations in terms of observational quantities, we obtain the following:

$$T_s = 0.77 T_x \ (10^6 \text{ K}) ,$$

$$v_s = 265 T_s^{1/2} \ (\text{km s}^{-1}) ,$$

$$n_0 = 7.58 \times 10^{-7} \left(\frac{\mathcal{F}_X}{\Lambda \theta_s^3 d} \right)^{1/2} \ (\text{cm}^{-3}) ,$$

$$E_{51} = 7.88 \times 10^{-17} T_s \left(\frac{\mathcal{F}_X \theta_s^3 d^5}{\Lambda} \right)^{1/2} \ (10^{51} \text{ ergs}) ,$$

$$t = 12.9 T_s^{-1/2} \theta_s d \ (\text{yr}),$$

and

$$M_s = 7.63 \times 10^{-14} \left(\frac{\mathcal{F}_X \theta_s^3 d^5}{\Lambda} \right)^{1/2} \ (M_\odot) ,$$

where observationally determined parameters are T_x, the X-ray spectral temperature in (10^6 K); θ_s, the SNR angular diameter in degrees; and $\mathcal{F}_X$, the X-ray flux (0.1–1.0 keV) in ergs cm^{-2} s^{-1}, corrected for interstellar absorption. We note that the flux correction for absorption introduces a large uncertainty into the ambient density, energy, time, and swept-up mass, since the X-ray absorption is not well-determined for these data and could be as much as an optical depth in the $\frac{1}{4}$ keV band. We have assumed column densities of 4.5×10^{19} cm^{-2} and 0 for EXE1 and EXE2, respectively. We have taken the angular diameters to be 20° for EXE1 and 5° for EXE2 (we note that the small angle approximation used to derive these relations is good to within 0.5% even for EXE1). T_s is the shock temperature in (10^6 K), v_s is the shock velocity, n_0 is the initial ambient density, d is the distance to the object in pc, E_{51} is the conserved energy, t is the age of the remnant, and M_s is the swept-up mass in the shell. Here Λ is the cooling function (0.1–1.0 keV), which we obtain directly from the Raymond & Smith plasma emission model by integrating over the appropriate energy range for the temperature that best fits the data.

To verify that the remnants are consistent with being in the adiabatic phase, we have also calculated the radii at which subsequent phases are expected to occur. The remnant radius at the time of onset of the pressure-driven snowplow phase, R_{PDS}, is given by Cioffi, McKee, & Bertschinger (1988) as

$$R_{PDS} = 14.0 E_{51}^{2/7} n_0^{-3/7} \zeta_m^{-1/7} \text{ pc} ,$$

while Cox (1972) gives the radius at onset of the radiative phase as

$$R_R = 26.4 E_{51}^{5/17} n_0^{-7/17} \text{ pc} .$$

We take the metallicity factor, ζ_m, to be 1 (solar abundances), but note that R_{PDS} is only weakly dependent on this term.

The results of these calculations are given in Table 5. The radii of both objects are consistent with being in the adiabatic phase if interpreted as SNRs; that is, their radii are less than R_{PDS}. The results for EXE1 show that the X-ray emission could be the result of a supernova event with a total energy in the range of $1–10 \times 10^{50}$ ergs, depending on its distance. In this case the X-ray emission is due to heating of the swept-up ISM by the shock. The shock velocity derived here exceeds the shell velocity observed at 21 cm by two orders of magnitude, and the presence of this shell is not expected for an adiabatic remnant. We suggest that the remnant is evolving inside a preexisting cavity carved out of the ISM by earlier SNRs or stellar winds (Chevalier & Liang 1989; Tenorio-Tagle et al. 1990), in which case the discrepancy between the shell velocity and the shock velocity is not surprising. Furthermore, this hypothesis can explain the large difference between the mass of the shocked medium obtained for the X-ray remnant and that of the neutral

TABLE 5

SEDOV MODEL PARAMETERS FOR TWO INDEPENDENT SNRS

Parameter	EXE1		EXE2	
T_s (10^6 K)	1.64		1.21	
v_s (km s^{-1})	339		291	
	d = 130 pc	d = 400 pc	d = 130 pc	d = 300 pc
n_0 (cm^{-3})	0.022	0.013	0.037	0.024
E_{51} (10^{51} ergs)	0.067	1.1	0.001	0.010
t (10^3 yr)	26.2	80.6	7.6	17.6
M_s ($M_\odot$)	39.3	652	1.0	8.3
R_{PDS}	33	94	8.6	19
R_R	57	164	14.5	32

shell, and also accounts for the low initial density found for EXE1.

The SNR model does not work so well for EXE2, since the explosion energy obtained is far less than that expected from an SN explosion for any reasonable distance. The remnant would have to be at a distance of 670 pc to be consistent with an energy of even 10^{50} ergs, which would place it 460 pc below the Galactic plane. This seems unlikely. Such a large distance is also probably incompatible with the low N_H determined by our spectral fit. We therefore conclude that EXE2 is not an adiabatic SNR.

4.4. *The Stellar Wind Bubble Interpretation*

We now consider whether the X-ray enhancements can be interpreted as independent stellar wind bubbles. The basic theory of stellar wind bubbles was developed by Castor, McCray, & Weaver (1975) and Weaver et al. (1977). Because the adiabatic phase is so short in a stellar wind bubble, we assume that the bubbles are in the radiative (snowplow) phase. In this case the X-ray emission arises from the shocked ISM in the interior of the bubble (region 2), and we have the following relations for this gas (Lamers 1983):

$$T_2 = 1.6 \times 10^6 L_w^{8/35} n_0^{2/35} t_6^{-6/35} \text{ (K)},$$

$$n_2 = 0.01 L_w^{6/35} n_0^{19/35} t_6^{-22/35} \text{ (cm}^{-3}\text{)},$$

and

$$\mathscr{L}_x = 3 \times 10^{33} L_w^{37/35} n_0^{18/35} t_6^{16/35} \text{ (ergs s}^{-1}\text{)},$$

where L_w is the wind luminosity in units of 10^{36} ergs s^{-1}, n_0 is the initial density in cm^{-3}, and t_6 is the bubble age in millions of years. Inverting these relations and recasting them in terms of the observationally determined quantities, we obtain the following expressions for the input parameters of the stellar wind bubble:

$$n_x = 1.21 \times 10^{-6} \left(\frac{\mathscr{F}_x}{\Lambda \theta_s^3 d} \right)^{1/2} \text{ (cm}^{-3}\text{)},$$

$$L_w = 2.90 \times 10^3 T_x^{10/3} \Lambda^{1/3} \theta_s \, d \text{ (}10^{36}\text{ ergs s}^{-1}\text{)},$$

$$n_0 = 2.66 \times 10^{-3} T_x^{-13/3} \Lambda^{-5/6} \theta_s^{-5/2} \mathscr{F}_x^{3/2} d^{1/2} \text{ (cm}^{-3}\text{)},$$

and

$$t_6 = 8.98 \times 10^4 T_x^{-17/6} \Lambda^{1/6} (\theta_s \mathscr{F}_x d^3)^{1/2} \text{ (}10^6\text{ yr)},$$

where we have made the approximation that the X-ray emission is produced in a region of uniform density, n_x, and uniform temperature, T_x.

The stellar wind bubble parameters obtained for EXE1 and EXE2 are given in Table 6. The density in the hot bubble interior derived from the model is much higher than that obtained directly from our observations (see Table 4). Otherwise, the parameters derived for EXE2 are within the range expected for a typical stellar wind bubble. The wind luminosity required to power this bubble requires a star of roughly 40 $M_\odot$ (Lamers 1983). Unfortunately, there are no massive stars within this object; the earliest type stars are HD 25631 (B3V, $d = 550$ pc) and HD 26326 (B5IV, $d = 250$ pc). Of these, only HD 26326 is located near the center of EXE2. Since the summed wind luminosity of both stars is insufficient to energize EXE2 by more than an order of magnitude, the nature of this object remains undetermined.

TABLE 6

STELLAR WIND BUBBLE PARAMETERS

Parameter	EXE1		EXE2	
	$d = 130$ pc	$d = 400$ pc	$d = 130$ pc	$d = 300$ pc
n_x (cm^{-3})	0.035	0.020	0.059	0.039
n_0 (cm^{-3})	18.9	33.2	20.2	30.7
L_w (10^{36} ergs s^{-1})	3.1	9.6	0.28	0.65
t_6 (10^6 yr)	2.3	12.5	0.56	1.98

EXE1 requires a somewhat more energetic wind of 3–10×10^{36} ergs s^{-1}, which is comparable to the total stellar wind luminosity of the Ori OB1 association (2×10^{37} ergs s^{-1}, Reynolds & Ogden 1979). This is consistent with the interpretation that the X-ray bubble fills a cavity created by this association, even if the cavity diameter is more like 40°, as suggested by Hα observations (Reynolds & Ogden 1979).

4.5. *Breakout of an SNR near a Molecular Cloud?*

If EXE1 and EXE2 are at the same distance, we can consider the interesting possibility that EXE2 is a supernova remnant caught in the act of breaking out into the Eridion Bubble and reheating it. Models of such interactions have been discussed by Tenorio-Tagle, Bodenheimer, & Yorke (1985) and have a morphology similar to that of the Eridanus enhancement. Because of the lower density in the preexisting cavity, the supernova remnant expands at a faster rate in the Eridion Bubble and can survive there for a longer time in the adiabatic phase compared with the evolution in the original cavity.

There are two significant problems with this interpretation. The first is that the observed temperature distribution ($T_{EXE1} > T_{EXE2}$) is the opposite of that produced by the models of Tenorio-Tagle et al. However, their models apparently assume an intercloud medium at 10^5 K, whereas the temperature inside the EXE1 cavity could have exceeded 10^6 K before EXE2 broke into it. With a higher initial temperature, it is possible that final temperatures in EXE1 could exceed those in EXE2. Furthermore, the hot lower density medium in EXE1 would cool more slowly than that in EXE2, which could help explain the temperature inversion. The second problem is that these models are for breakout from a molecular cloud, but there is no indication of a molecular cloud associated with EXE2, or even a very significant neutral cloud. The nearest known molecular cloud is MBM20 at (l, b) = (210°.9, −36°.5), about 6°.5 from the center of EXE2.

If the "breakout" occurred from a diffuse neutral cloud instead of from a dense molecular cloud, the SNR would evolve less rapidly and would grow to a larger size in the adiabatic phase than for the cases modeled by Tenorio-Tagle et al. The breakout into a low-density cavity could then account for the low apparent explosion energy for EXE2, since much of the shock energy would then be lost to reheating the cavity. However, we consider this model to be somewhat contrived and unnecessarily complex for this object.

4.6. *A Model for the Eridion Bubble*

In Figure 9 we sketch a model for this part of the sky that is consistent with all of the observations described above. The region is shown in two directions orthogonal to the plane of the sky: Figure 9*a* shows a cross section perpendicular to the Galactic plane and viewed from the right-hand side of our sky images, while Figure 9*b* shows a view looking down on this region from the Galactic plane. The sketch is dominated by the

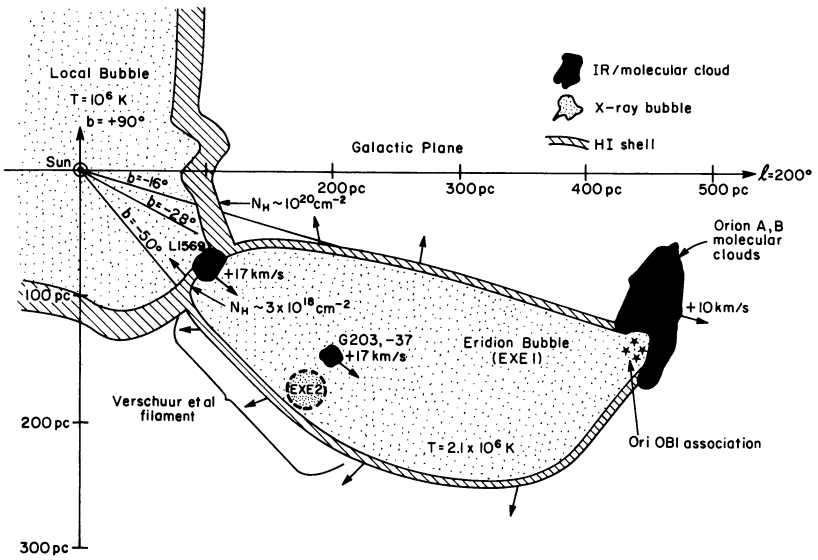

FIG. 9*a*

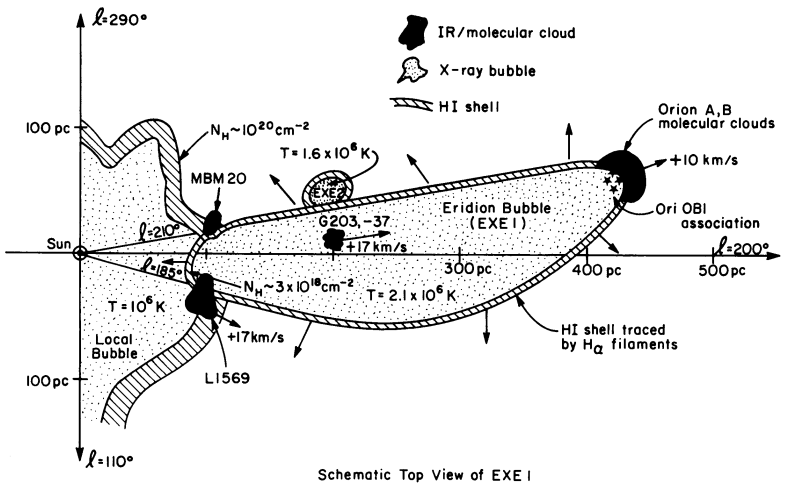

FIG. 9*b*

FIG. 9.—Sketch of the Eridanus region, approximately to scale. (*a*) Schematic "vertical" cross section of EXE1 along Galactic longitude 200°, showing the proposed relationship between the X-ray emitting cavity, the Local Bubble surrounding the Sun, and the molecular clouds and N_H filaments that surround the X-ray cavities. (*b*) Top view (looking down from the Galactic plane) of the same schematic picture of the Eridanus enhancement.

Eridion Bubble. Our sketch of this object is very similar to Figure 6 of Reynolds & Ogden (1979), but we have placed the near side of the bubble closer to the Sun to allow it to interact with L1569. This sketch is certainly not a unique model, even given the observational constraints. Much of the crucial information, such as the distances to the near and far edge of the cavity, is only hinted at circumstantially. Although this sketch presents our best attempt to bring together all of the data at hand to form a consistent picture, it is worthwhile to reiterate which features of this picture are fairly well established and to discuss why the figure is drawn as it is.

We begin by assuming that the X-ray emission outlines the Eridion Bubble. Our X-ray data can then locate the edges of this bubble in latitude and longitude over the region covered by our maps. This allows us to sketch in the southern boundary of the bubble along $b = -50°$ in Figure 9*a*, and to sketch in the sides as bounded by $l = 185°$ and $l = 210°$ in Figure 9*b*. We have made the assumption that the bubble continues north to Orion and have sketched the northern boundary accordingly. (This is consistent with lower resolution *HEAO 1* maps and earlier maps made by the Wisconsin group [Williamson et al. 1974]. It also provides the absorption-free path needed to account for the enhanced Hα emission seen in the Eridanus region [Reynolds & Ogden 1979]).

We have drawn the Local Bubble with the shape determined by Snowden et al. (1990), but have arbitrarily scaled the cavity size so that it intersects the near edge of the Eridion Bubble. (This scaling is intermediate between the extremes shown in Snowden et al.) There is no evidence for any interaction between the two cavities, but this picture provides a natural explanation for the very low intervening column density.

We have assumed a column density of about 1×10^{20} cm^{-2}

for the shell of the Local Bubble. This column density is consistent with Lyman α and optical absorption line measurements of column densities toward stars within several hundred parsecs of the Sun (Frisch & York 1983). It provides a column sufficient to absorb $\frac{1}{4}$ keV X-rays (L1 and L2 bands) from the bubble for latitudes above $b = -28°$ while transmitting the higher energy M1 band X-rays, if the walls of the Local Bubble and the Eridion Bubble intersect at about $-28°$ latitude as shown in Figure 9*a*. The near side of the Eridion Bubble has a much lower column density of only 3×10^{18} cm^{-2} as determined by the column density derived from 21 cm maps at the velocity of the cap of the expanding shell. This column density is also consistent with our X-ray spectral fits. We note that the elongated shape of the cavity shown in Figure 9 may explain the inconsistency noted in § 3.3 between the shell mass derived from the bounding filaments and that derived from the cap, since those numbers were derived assuming a spherical cavity. The shape suggested here will provide a much higher column density for the tangentially viewed portions of the shell than that deduced from the column density in the cap, even for a uniform shell density.

We have placed L1569 at its known location in space and have made the assumption (based on the fact that a prominent Hα filament is associated with this cloud) that the Eridion Bubble is interacting with it. This accounts for the Hα emission by allowing UV photons from Orion to ionize the back side of this cloud and allows the shock front from the Eridanus Bubble to produce the filamentary structures seen in L1569 as it engulfs the cloud. This relationship also permits L1569 to absorb the soft X-rays from the bubble, thereby accounting for both the apparent hook-shaped appearance of the Eridanus enhancement and for the apparent absorption along the north edge of L1569.

We have also placed MBM20 at the interface between the Local Bubble and the Eridion Bubble, although we have no distance estimate for this cloud. It might seem somewhat unlikely that two high-latitude molecular clouds should happen to be located between these two bubbles, but we suggest that the interaction of the shock fronts of the Local Bubble and the Eridion Bubble may be responsible for the compression of the H I shells and the formation of these two molecular clouds in these locations. The N_H/IR filament extending north from MBM 20 may be the $l = 210°$ neutral wall of the Eridion Bubble seen tangentially, as noted above, while the southern cavity wall, also viewed tangentially, could be the Verschuur et al. filament (Verschuur et al. 1992).

We have placed the cloud we labeled G203$-$37 in the interior of the cavity. This placement is speculative, but we do know that this cloud does not absorb the $\frac{1}{4}$ keV X-rays, that it in fact coincides with a $\frac{1}{4}$ keV peak with a lower temperature than average, and that the edges of this cloud appear to be heated. All of these observations are consistent with its placement in the interior of the Eridion Bubble, with the cloud evaporating and cooling the hot gas in its interior.

Our picture shows the Ori OB1 association carving out a caviy in the Orion A and B molecular clouds. We suggest that this cavity may be responsible for channeling the stellar winds and supernova blast waves in our general direction, and hence for the elongated shape of the Eridion Bubble. The higher density toward the Galactic plane could also contribute to the location of the northern boundary of the bubble (which our observations do not locate). It is less clear why the bubble should not continue to extend further to the south, where one would expect lower densities to favor a more rapid expansion, but we are constrained by our X-ray observations, which show a sharp boundary to the southern edge of the bubble at a Galactic latitude of about $-50°$.

5. CONCLUSIONS

We have considered a variety of models for the Eridanus soft X-ray enhancement. We find that the main enhancement, EXE1, can be explained as either an adiabatic supernova remnant roughly $53 \pm 27 \times 10^3$ years old which expanded into a region of density 0.01–0.02 cm^{-3}, or as a stellar wind bubble with age 2–12 $\times 10^6$ years and initial density 20–30 cm^{-3}. If EXE1 is interpreted as a supernova remnant, it requires an unusually low initial density, suggestive of a preexisting cavity. If interpreted as a stellar wind bubble, the bubble parameters are quite reasonable if the bubble is energized by the Ori OB1 association. These same stars appear to provide the ionizing flux necessary to produce the Hα observed by Reynolds & Ogden (1979) and so are probably associated with this object. Given the apparent presence of the Ori OB1 association within this bubble, a likely scenario is that the Eridanus enhancement is produced by a nearby superbubble energized by the combined effects of stellar winds and supernova explosions from the Ori OB1 association. A sketch of this Eridion Bubble is shown in Figure 9.

Further evidence supporting this view comes from the Hα and 21 cm velocity data. The H I filaments that bound EXE1 are moving at negative velocities, with the largest cavity extent appearing between -15 and -5 km s^{-1}. The molecular clouds associated with the Ori OB1 association are moving away from us at $\sim +10$ km s^{-1} (Maddalena et al. 1986) and are located at a distance of about 450–500 pc. If the bubble has expanded toward us, as suggested by the relatively close apparent distance of its near side, the portions of the shell tangential to our line of sight should have a negative radial velocity, consistent with the observations. Our model of the bubble also accounts for the asymmetric velocity spreading found by Reynolds & Ogden, since for a given line of sight, the near side of the bubble is expanding more nearly along the line of sight than the far side; hence the negative radial velocities should exceed the positive velocities from the far shell, as observed.

EXE2 does not fit the adiabatic SNR picture because the required explosion energy is too small to explain as a SNR unless this object is extemely distant. EXE2 does fit the stellar wind bubble model quite well. However, there is no obvious candidate for the source of the energizing flux, since the object contains no O stars and only two B stars with insufficient wind luminosity to account for the X-ray flux that we observe. A third possibility is that EXE2 is simply a small-scale blowout of EXE1 near its southern boundary where the bounding shell might be very thin. Perhaps the cooler temperature in EXE2 is due to adiabatic cooling of the gas as it ruptures the wall of EXE1. However, this may not be consistent with the thermal pressures, since the pressure in EXE1 is only 9000 cm^{-3} K for the geometry shown in Figure 9, while the pressure in EXE2 appears to be 2–3 times higher. The nature of this object remains an open question and will require further study.

Although the superposition of EXE1 and EXE2 on the sky suggests that they may be interacting, we find no evidence other than their proximity on the sky to support this hypothesis. These objects do not appear to have the characteristics expected for interacting supernova remnants, and we believe that their juxtaposition on the sky is fortuitous. Nevertheless,

the geometry of the two objects places them in close spatial proximity unless EXE2 is a very distant SNR, as we have shown in Figure 9.

The Eridanus enhancement is a rich and complex object that would benefit from detailed study with higher angular resolution. The *ROSAT* sky survey can provide such data at X-ray wavelengths with higher angular resolution and sensitivity than was possible with the *HEAO 1* A-2 LEDs. The *ROSAT* data will be well matched to the full angular resolution of the *IRAS* data, and we expect these data to provide a more definitive analysis of the Eridanus enhancement and to resolve some of the remaining questions and ambiguities. In particular, sensitive X-ray spectra of critical regions of the enhancements will be crucial in unraveling the spatial relationships between the hot and cold components of this complex region. Improved distances to the cold clouds and filaments associated with the bubble are also needed.

We thank George Weaver for his assistance in preparing the *HEAO 1* maps used for this analysis; Carl Heiles for providing us with the Crawford Hill 21 cm data; and Don Cox, Dick Edgar, David Leisawitz, Bryan Penprase, and an anonymous referee for useful comments. This work was supported by NASA grants NAG5-941, NAG5-100, NAG8-758, and NAG8-478 and by JPL contract 657268.

REFERENCES

Boulanger, F. 1989, in The Physics and Chemistry of Interstellar Molecular Clouds, ed. G. Winnewisser & J. T. Armstrong (Berlin: Springer), 30
Boulanger, F., & Pérault, M. 1988, ApJ, 330, 964
Castor, J., McCray, R., & Weaver, R. 1975, ApJ, 200, L107
Chevalier, R. A., & Liang, E. P. 1989, ApJ, 344, 332
Cioffi, D. F., McKee, C. F., & Bertschinger, E. 1988, ApJ, 334, 252
Cox, D. P. 1972, ApJ, 178, 159
Explanatory Supplement to the *IRAS* Catalogs and Atlases 1987, ed. C. A. Beichman, G. Neugebauer, H. J. Habing, P. E. Clegg, & T. J. Chester (Washington: GPO)
Fink, R. L. 1990, Ph.D. thesis, Penn State Univ.
Franco, G. A. P. 1988a, A&AS, 74, 73
———. 1988b, A&A, 202, 173
Frisch, P. C., & York, D. G. 1983, ApJ, 271, L59
Garmire, G. P., Nousek, J. A., Apparao, K. M. V., Burrows, D. N., Fink, R. L., & Kraft, R. P. 1992, ApJ, 399, 694
Gull, S. F., & Daniell, G. J. 1978, Nature, 272, 636
Hamilton, A. J. S., Sarazin, C. L., & Chevalier, R. A. 1983, ApJS, 51, 115
Heiles, C. 1976, ApJ, 208, L137
Heiles, C., & Habing, H. J. 1974, A&AS, 14, 1
Lamers, H. J. G. L. M. 1983, in Diffuse Matter in Galaxies, ed. J. Audouze et al. (Dordrecht: Reidel), 45
Lampton, M., Margon, B., & Bowyer, S. 1976, ApJ, 208, 177
Long, K. S., Patterson, J. R., Moore, W. E., & Garmire, G. P. 1977, ApJ, 212, 427
Maddalena, R. J., Morris, M., Moscowitz, J., & Thaddeus, P. 1986, ApJ, 303, 375
Marshall, F. J., & Clark, G. W. 1984, ApJ, 287, 633
McCammon, D., Burrows, D. N., Sanders, W. T., & Kraushaar, W. L. 1983, ApJ, 269, 107
Murthy, J., Im, M., Henry, R. C., & Holberg, J. B. 1992, ApJ, submitted
Naranan, S., Shulman, S., Friedman, H., & Fritz, G. 1976, ApJ, 208, 718
Neugebauer, G., et al. 1984, ApJ, 278, L1
Nousek, J. A., Fried, P. M., Sanders, W. T., & Kraushaar, W. L. 1982, ApJ, 258, 83
Nugent, J. J., et al. 1983, ApJS, 51, 1
Paresce, F., Jakobsen, P., & Bowyer, S. 1983, A&A, 124, 300
Penprase, B. E., Blades, J. C., Danks, A. C., & Crane, P. 1990, ApJ, 365, 241
Puget, J. L., & Léger, A. 1989, ARA&A, 27, 161
Rappaport, S., Doxsey, R., & Solinger, A. 1974, ApJ, 194, 329
Raymond, J. C., & Smith, B. W. 1977, ApJS, 35, 419
———. 1990, private communication (update to Raymond & Smith 1977)
Reynolds, R. J., & Ogden, P. M. 1979, ApJ, 229, 942
Rothschild, R., et al. 1979, Space Sci. Instr., 4, 269
Singh, K. P., Manchanda, R. K., Naranan, S., & Sreekantan, B. V. 1982, Astrophys. Lett., 23, 47
Singh, K. P., Nousek, J. A., Burrows, D. N., & Garmire, G. P. 1987, ApJ, 313, 185
Sivan, J. P. 1974, A&AS, 16, 163
Snowden, S. L., Cox, D. P., McCammon, D., & Sanders, W. T. 1990, ApJ, 354, 211
Stark, A. A., Gammie, C. F., Wilson, R. W., Bally, J., Linke, R. A., Heiles, C., & Hurwitz, M. 1992, ApJS, 78, 77
Tenorio-Tagle, G., Bodenheimer, P., Franco, J., & Różycxka, M. 1990, MNRAS, 244, 563
Tenorio-Tagle, G., Bodenheimer, P., & Yorke, H. W. 1985, A&A, 145, 70
Verschuur, G. L., Rickard, L. J., Verter, F., Pound, M. W., & Leisawitz, D. 1992, ApJ, 390, 514
Walter, F., Charles, P., & Bowyer, S. 1978, Nature, 274, 569
Weaver, R., McCray, R., Castor, J., Shapiro, P., & Moore, R. 1977, ApJ, 218, 377
White, N. E., & Sanford, P. W. 1978, Nature, 274, 569
Williamson, F. O., Sanders, W. T., Kraushaar, W. L., McCammon, D., Borken, R., & Bunner, A. N. 1974, ApJ, 193, L133
Willingale, R. 1981, MNRAS, 194, 359